Journal of Structural Geology 178 (2024) 105012

Contents lists available at ScienceDirect

Journal of Structural Geology

journal homepage: www.elsevier.com/locate/jsg

Magnetic multi-fabrics as tools for understanding ignimbrite emplacement processes: An example from late-Variscan Tharandter Wald Caldera, Bohemian Massif

Irena Olšanská [a,*], Filip Tomek [a,b], Martin Chadima [b,c], Marine S. Foucher [d], Michael S. Petronis [d]

[a] Institute of Geology and Paleontology, Faculty of Science, Charles University, Albertov 6, Prague, 12843, Czech Republic
[b] The Czech Academy of Sciences, Institute of Geology, Rozvojová 269, Prague, 16500, Czech Republic
[c] AGICO Inc, Ječná 29a, 621 00, Brno, Czech Republic
[d] Environmental Geology, Natural Resources Management Department, New Mexico Highlands University, Las Vegas, NM, 87701, USA

ARTICLE INFO

Keywords:
Bohemian Massif
Collapse caldera
Ignimbrite
Magnetic anisotropy
Rhyolite

ABSTRACT

Felsic collapse calderas pose a hazard to our society, thus detailed knowledge of collapse mechanisms and behavior of eruptive products could help us to better understand the active calderas. We present a model of the eruption and collapse of Late Carboniferous Tharandter Wald Caldera (Variscan Bohemian Massif) based on field mapping and a magnetic multi-fabric approach. We investigate intra-caldera rhyolitic ignimbrites using a combination of conventional in-phase and relatively new out-of-phase anisotropy of magnetic susceptibility, along with the anisotropy of anhysteretic remanent magnetization. A two-stage caldera evolution model is proposed. (1) The high-energetic and high-temperature ignimbrites filled the paleo-valleys to form a thick ignimbrite sheet with welded to rheomorphosed central portion. Concurrently, eruptions emptied the source magma chamber triggering the piston caldera collapse. (2) The subsidence caused a monoclinal ductile bending of the still-hot and ignimbrite sheet around the caldera rim towards its center. Caldera activity was terminated by the emplacement of subvolcanic ring and radial dikes associated with hydrothermal activity. The latter likely induced abundant magneto-mineralogical alteration and formed composite fabrics. Hence, the application of the multi-fabric approach may serve as a useful tool to extrapolate reliable geodynamic proxies from the magnetic fabric of old, eroded, or altered caldera ignimbrites.

1. Introduction

Field and structural studies complemented by the anisotropy of magnetic susceptibility are well-proven and established methods for studying the emplacement processes of ignimbrites (Wang et al., 2001; Ort et al., 2003; Porreca et al., 2003; Agrò et al., 2015; Platzman et al., 2020). Ignimbrites are deposits of high-energetic pyroclastic density currents (PDC) mostly produced by explosive volcanic eruptions at felsic calderas and stratovolcanoes (Wilson and Walker, 1982; Walker, 1983; Druitt, 1998; Branney and Kokelaar, 2007; Dufek et al., 2015). Ignimbrite deposits include various compositions ranging from ash-dominated, through pumice- or scoria-dominated, to crystal-rich pyroclastic rocks, contain lithic clasts, may have several degrees of welding, and vary in thickness, volume, and aerial extent (Sparks et al., 1973; Branney and Kokelaar, 2007; Giordano and Cas, 2021). While some ignimbrite deposits include multiple petrographic markers such as cross-bedding and flow foliations that allow direct interpreting emplacement dynamics, others appear macroscopically isotropic. In such cases, rock-magnetic techniques such as the anisotropy of magnetic susceptibility (AMS) and/or anisotropy of anhysteretic remanent magnetization (AARM) are useful tools to define the internal preferred orientation of magnetic minerals and thus reconstruct the magnetic fabrics (Hrouda, 1982; Borradaile, 1987, 2001; Tarling and Hrouda, 1993; Borradaile and Jackson, 2010). Apart from magnetic foliations and lineations, the magnetic fabric also allows direct quantification of the mean (volumetric) magnetic susceptibility roughly reflecting mineral rock compositions, degree of anisotropy suggesting the fabric intensity, and shape parameter indicating the symmetry of fabric ellipsoids. It is well-established that the magnetic fabric yields valuable information on PDC flow directions at different scales, source vent

* Corresponding author.
E-mail address: olsanski@natur.cuni.cz (I. Olšanská).

https://doi.org/10.1016/j.jsg.2023.105012
Received 6 June 2023; Received in revised form 16 November 2023; Accepted 19 November 2023
Available online 28 November 2023

localization, post-emplacement processes, and overall time-transgressive volcano paleoreconstructions (e.g., Cagnoli and Tarling, 1997; MacDonald et al., 2012; Ort et al., 2015; Simón-Muzás et al., 2022). As such, ignimbrites commonly yield shallowly dipping magnetic and/or macroscopic foliations associated with down-dip or strike-parallel lineations along with the oblate shape of the fabric ellipsoid referred to as normal magnetic fabric. The angle between foliation and ignimbrite basal plane records mineral imbrication caused by PDC flow and emplacement dynamics (see for instance Ellwood, 1982; Fisher et al., 1993; Ort et al., 2003; Giordano et al., 2008; Agrò et al., 2015 among many others). However, in some cases, the primary fabric record could be obscured by overprinting welding and rheomorphism, tectonic deformation, and mineral alteration, superposition of which may lead to the formation of composite and/or inverse magnetic fabrics (e.g., Wang et al., 2001; Geissman et al., 2010; Ort et al., 2015). Moreover, at some relatively older caldera complexes of the Paleozoic or even older age, only deep erosional reliefs are preserved (e.g., Wang et al., 2001; Willcock et al., 2015; Vitouš et al., 2022).

In this manuscript, we present a new structural dataset that combines field and structural mapping along with the magnetic multi-fabrics complemented with a detailed rock-magnetic investigation of high-grade rhyolitic ignimbrites of the late Carboniferous Tharandter Wald Caldera, northwestern Bohemian Massif (European Variscan belt). The multi-fabric approach utilizes conventional low-field in-phase anisotropy of magnetic susceptibility (ipAMS) and AARM supported by a newly introduced out-of-phase anisotropy of magnetic susceptibility (opAMS) technique capable of distinguishing magnetic fabrics carried by ultra-fine ferromagnetic grains (Hrouda et al., 2017, 2020, 2022). To specify the carriers of magnetic fabrics, we applied several magneto-mineralogical tests including the thermomagnetic susceptibility curves, frequency-dependent susceptibility, hysteresis loops, first-order reversal curves, and optical and electron microscopy. The application of magnetic multi-fabric along with the detailed magneto-mineralogical tests allowed us to isolate some magnetic fabric data that resulted from hydrothermal alteration and the formation of composite fabrics. The fabric pattern of high-grade rheomorphic ignimbrite is interpreted as formed in two-steps. First, the pyroclastic density currents deposited an extensive and thick ignimbrite sheet with intensely welded and in places rheomorphosed proximal facies in the area of the future caldera. Second, the drainage of the source magma chamber triggered the caldera collapse, which in turn caused a ductile monoclinal bending of still-hot and ductile ignimbrites along the caldera margins.

2. Regional geologic setting in brief

The Bohemian Massif is the largest exposure of the Variscan orogenic belt in Europe (Matte et al., 1990; Matte, 1991; Winchester, 2002; Schulmann et al., 2014; Žák et al., 2014). The Variscan orogeny formed as a result of oblique convergence and final collision between northern Gondwana and southern Laurussia mainlands along with several microplates sutured between the converging plates. The incipient collision closed the Rheic Ocean and other smaller oceanic domains during the Devonian and Carboniferous periods (Franke, 1989, 2006; Pin, 1990; Pharaoh, 1999; Winchester et al., 2006; Edel et al., 2013, 2018; Schulmann et al., 2014).

In the Bohemian Massif, the subduction and closure of the Saxothuringian ocean were followed by the collision of the Saxothuringian and Teplá-Barrandian microplates between ~380 Ma and 346 Ma (Schäfer et al., 1997; Žák et al., 2005, 2012, 2014; Schulmann et al., 2009, 2014). The ~346–335 Ma orogenic collapse resulted in the rapid exhumation of the lower and middle crust, now exposed as the Moldanubian unit (Dörr and Zulauf, 2010; Žák et al., 2014). A rather exotic terrane of likely Avalonian affinity, the Brunovistulian microplate, was underthrusted beneath the Moldanubian and Saxothuringian units along the eastern margin of the Bohemian Massif at ~344–335 Ma (Schulmann and Gayer, 2000; Racek et al., 2017). The orogenic collapse triggered major tectonothermal processes in the peripheral areas of the Bohemian Massif resulting in the production of voluminous early ultrapotassic and high-K plutons, and late S-type and high-K I-type granites emplaced between ~335 Ma and 315 Ma (Förster et al., 1999; Finger et al., 2009, 2022, Žák et al., 2013, 2014; Verner et al., 2014; Janoušek et al., 2020; Tichomirowa et al., 2019; Megerssa et al., 2023). Magmatism is thought to be linked to decompression melting, mantle heat addition due to slab delamination, and/or the presence of large volumes of ponded mafic magma at depth, which facilitated large-scale crustal anatectic melt generation (Gerdes et al., 2000; Finger et al., 2009, 2022; Žák et al., 2011, 2014; Janoušek et al., 2020). Concurrently, the dextral strike-slip movements along major ~ NW–SE striking crustal-scale shear/fault zones occurred (e.g., Intra Sudetic Fault, Elbe, Danube, and Pfahl zones; Aleksandrowski, 1997; Scheck et al., 2002; Käßner et al., 2021; Megerssa et al., 2023). This process was closely associated with the development of the intramontane, coal-bearing Carboniferous basins (e.g., Opluštil and Cleal, 2007; Opluštil et al., 2016b; Martínek et al., 2017). The sedimentary fill is often intercalated with Westphalian ash-fall tuff layers and volcaniclastic deposits (Ulrych et al., 2006; Opluštil et al., 2016a, 2016b; Tomek et al., 2022). However, only in the western part of the Saxothuringian unit in the NW Bohemian Massif, two large volcanic edifices, the Altenberg–Teplice and Tharandter Wald calderas along with some smaller eruptive centers related to this late Variscan event, are exposed (Benek, 1980; Breitkreuz et al., 2021; Tichomirowa et al., 2022; Tomek et al., 2022).

3. Tharandter Wald Caldera: an overview

3.1. Caldera geometry, geological relations, and emplacement

The Tharandter Wald Caldera (TWC; also variously referred to as Tharandt caldera, Tharandt forest caldera, or Tharandter volcanic complex) is a ~52 km^2 large and elliptical (~NE–SW striking longest axis) volcano-plutonic complex in the NW Bohemian Massif (Fig. 1). The TWC belongs to a ~NW–SE striking chain of late Paleozoic volcanic centers, which roughly delineate the Elbe shear/fault zone (Tröger et al., 1968). These include from north to south the Meissen volcanic complex (~303 Ma, U–Pb on zircons; Hoffmann et al., 2013), the TWC and the associated Niederbobritzsch pluton (~319–312 Ma, U–Pb on zircons; Breitkreuz et al., 2021), the Schönfeld–Altenberg complex, the Fláje pluton, and the Altenberg–Teplice Caldera (~325–312 Ma, U–Pb on zircons; Tichomirowa et al., 2022; Tomek et al., 2022). According to Benek (1980), the formation of these complexes was driven by dextral shearing along crustal-scale shear/fault zones with maximum horizontal shortening in the ~N–S direction. This hypothesis was recently corroborated by Tomek et al. (2023), who presented a detailed structural model of the emplacement of the Altenberg–Teplice Caldera. Note that the climactic eruptive activity of both the adjacent calderas yielded virtually the same age of ~314–313 Ma (Breitkreuz et al., 2021; Tichomirowa et al., 2022; Tomek et al., 2022). TWC was emplaced into crystalline complexes of the Precambrian to early Paleozoic age. These include the Freiberg gneiss dome (paragneiss, orthogneiss, and meta-graywacke) and Nossen Wilsdruff mountains (phyllite and slate; Gehmlich et al., 2000; Tichomirowa et al., 2001, 2012) that are bounded by the Hartha thrust fault.

The activity of the TWC magmatic system commenced with the intrusion of the pre-caldera Niederbobritzsch pluton (Fig. 1). Caldera evolution started with the eruption and deposition of ash-fall tuffs at the base of the caldera fill. The voluminous intra-caldera rhyolitic-ignimbrites erupted during the piston caldera collapse, while the outflow facies are not exposed at the present-day erosional level (Breitkreuz et al., 2021). The intra-caldera rhyolitic-ignimbrites are traditionally divided into two lithotypes. The more voluminous and relatively older quartz phenocryst-poor ignimbrite (hereafter referred to as Qz-poor ignimbrite) occupies about two-thirds of the present-day erosional

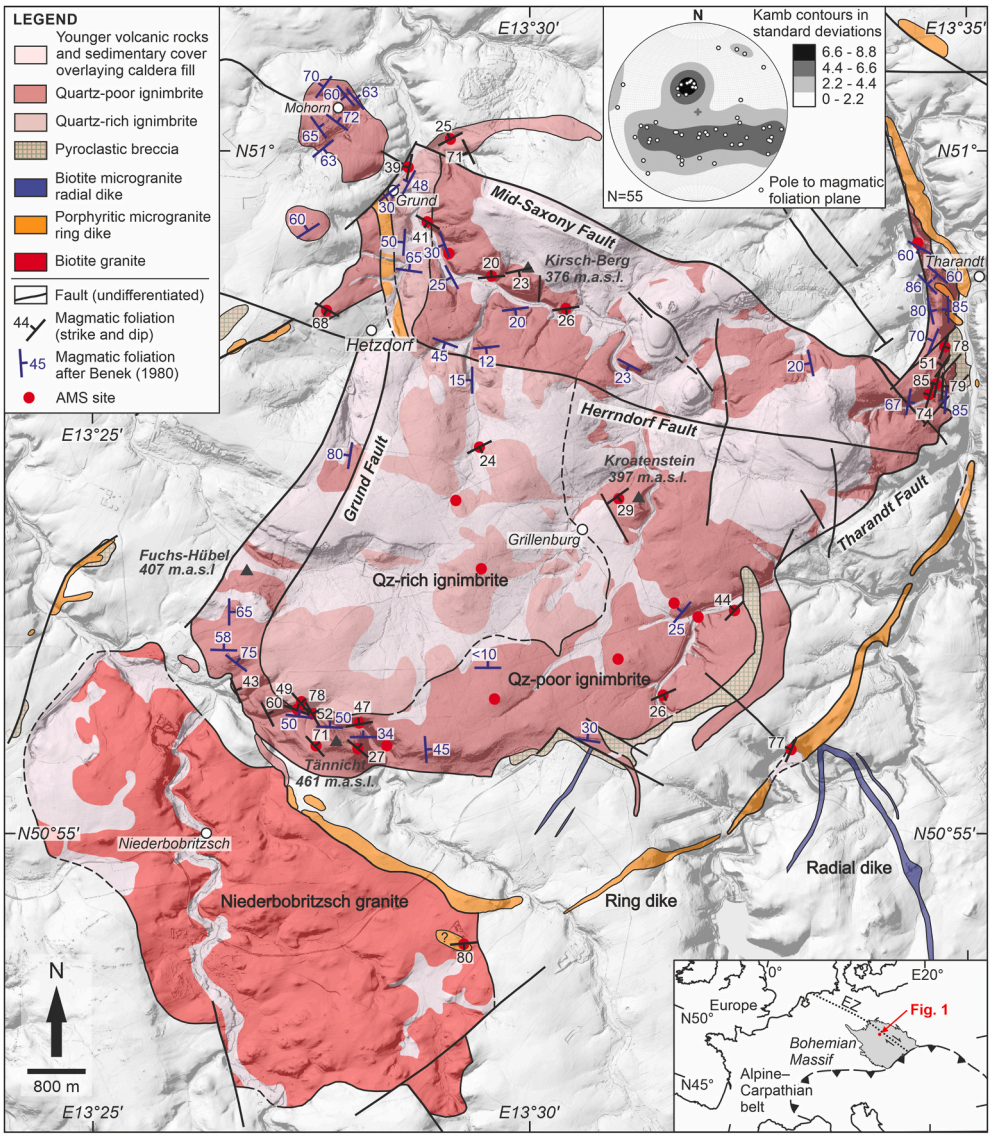

Fig. 1. A simplified geologic map of the Tharandter Wald Caldera and Niederbobritzsch pluton compiled from Benek (1980) and geologic maps in the scale of 1:25, 000 sheets 5046 Freiberg, and 5047 Freital (authorship not specified). A shaded relief base map was obtained through the WMS services of the Saxon State Office for Environment, Agriculture, and Geology. Equal area stereographic projection on a lower hemisphere of the pole of the magmatic foliation is also reported. Note the location of specimens for multi-fabric analysis shown by a red circle; See the supplementary material for WGS84 coordinates. The inset portrays the location of the Tharandter Wald Caldera in the Bohemian Massif. EZ – Elbe Zone. (For interpretation of the references to color in this figure legend, the reader is referred to the Web version of this article.)

surface. The younger and overlying lithotype is the less-voluminous quartz phenocryst-rich ignimbrite (Qz-rich ignimbrite), which is exposed in the central and western portions of the caldera (Fig. 1; Benek 1980). No field evidence of a depositional break between these two lithotypes occurs, suggesting emplacement during a single eruptive event (Breitkreuz et al., 2021).

A monolithic gneiss mesobreccia with a pyroclastic matrix occurs in the peripheral areas of the caldera fill and is interpreted as syn-collapse landslides (Fig. 1). In addition, some minor and isolated areas of lithic-rich ignimbrites and vitrophyric rhyolites were identified (Breitkreuz et al., 2021). Based on subsurface drilling data and field mapping, the minimum thickness of the preserved caldera fill is estimated to be 371 m, the minimum areal extent of pyroclastic deposits is 550 km^2, and the minimum cumulative volume of erupted material is estimated to be 22 km^3 (Benek, 1980; Breitkreuz et al., 2021). The caldera fill was intruded by the microgranite ring and radial dikes (Fig. 1; Benek 1980).

The TWC is cut by several major faults, including Herrndorf, Grund, Tharandt, and Mid-Saxony. About one-third of the caldera is disconformably overlayed by the Late Cretaceous sediments, intruded by Oligocene to Miocene basalts, and partly also covered by Quaternary sediments (Fig. 1).

3.2. Geochemistry and petrography of ignimbrites

The petrographical and geochemical datasets of Benek (1980) and Breitkreuz et al. (2021) reported that the TWC ignimbrites are silica-rich rhyolites (~75 wt% SiO_2). Both ignimbrite lithotypes share a similar whole-rock geochemical signature as well as the REE pattern with a negative anomaly in Ba, Sr, Ca, and Ti (Breitkreuz et al., 2021). The geochemistry also suggests that the Qz-poor ignimbrite represents the most evolved part of the underlying magma chamber, while the Qz-rich ignimbrite is characterized as a moderately evolved melt with an intermediate degree of fractional crystallization. The compositions of the pre-caldera Niederbobritzsch pluton together with the post-caldera ring

and radial dikes then correspond to the least evolved part of the source magmatic system (Breitkreuz et al., 2021).

The intra-caldera fill consists of the welded rhyolitic ignimbrites with variable amounts of quartz, plagioclase, K-feldspar phenocrysts, and minor biotite (Fig. 2c and d). The dominant Qz-poor ignimbrite contains up to 10–13% of crystals, whereas the Qz-rich ignimbrite includes up to 33% of quartz and feldspar phenocrysts (Benek 1980; Breitkreuz et al., 2021). In several parts of the caldera, the ignimbrites include also elongated fiamme and lithic clasts (Benek 1980; Breitkreuz et al., 2021). The lithic clasts are dominated by slates in the northern part, whereas in the southern part, they include mostly gneiss, schist, and volcanic clasts (Breitkreuz et al., 2021). Map trends reveal a spatial pattern in the volume and size of fiamme, and the occurrence of columnar joints in both ignimbrite lithotypes (Benek, 1980). In general, the volume and size of fiamme and the occurrence of columnar cooling joints decrease from the peripheral areas toward the caldera center (Benek, 1980).

4. Magnetic multi-fabric methodology

4.1. Sampling strategy

Detailed field and structural mapping at a scale of 1:10,000 was conducted in the TWC and the surrounding areas that are intruded by ring and radial dikes. Apart from structural data, we have collected 16 representative specimens for petrographic thin-sections, which were analyzed using optical and scanning electron microscopy. The specimens for rock magnetic experiments were obtained at 32 sampling sites in both the ignimbrite lithotypes and porphyritic microgranite ring dikes. The sites were selected to cover the entire exposed erosional surface of the caldera. We obtained either oriented drill core samples using a portable gasoline-powered drill or oriented block samples that were drilled in the laboratory. The core samples were cut into standard right-cylinder specimens (2.54 cm diameter × 2.20 cm height). From the 495 specimens collected (at least 8 specimens per site), 362 specimens (24 sites) were obtained from the Qz-poor ignimbrite, 99 specimens (6 sites) from Qz-rich ignimbrite, and 34 specimens (2 sites) from the ring dikes. The latter includes porphyritic microgranite at site TC62 situated within the Niederbobritzsch pluton (eastern margin) and may potentially represent a dike unrelated to the ring dikes.

Out of the 32 AMS sites, 17 representative sites (101 specimens, ~6 specimens per site) across the caldera were selected for AARM analysis. Magneto-mineralogical tests included specimens from 31 sites across the caldera for the analysis of frequency-dependent susceptibility, 10 sites for thermomagnetic curves (one representative powdered specimen per site was selected), and 17 representative specimens (chip fragments) for the hysteresis loops and first-order reversal curve (FORC) distributions. The results are presented in Figs. 4–11, while full data tables and complementary figures are provided in Supplementary Material items S1–S6. The readers are referred to Table 1 for an overview of the magnetic fabric parameters, magnetic mineralogy, and associated references.

4.2. Anisotropy of in-phase and out-of-phase magnetic susceptibility

Magnetic anisotropy is the directional variability of the magnetic susceptibility of minerals and rocks and provides an effective tool for recognizing internal rock fabrics that lack visible macroscopic structural features (Hrouda 1982; Tarling and Hrouda, 1993; Borradaile and Henry 1997; Borradaile and Jackson 2004, 2010). The AMS allows the interpretation of the flow and emplacement dynamics of subvolcanic dikes, sheets, and laccoliths (e.g., Knight and Walker, 1988; Petronis et al., 2004; Chadima et al., 2009; Burchardt et al., 2019; Tomek et al., 2019), lava flows and domes of different compositions (e.g., Loock et al., 2008; Závada et al., 2009; Akkoyun et al., 2013; Tomek et al., 2016; Kolářová et al., 2022; Prival et al., 2022), and pyroclastic rocks (e.g., Gountié Dedzo et al., 2011; Agrò et al., 2015; Ort et al., 2015; Moncinhatto et al., 2020; Vitouš et al., 2022).

In addition to quantifying the internal rock fabrics (K_1, maximum principal susceptibility axis = magnetic lineation; K_3, minimum principal susceptibility axis = pole/normal to magnetic foliation), AMS also

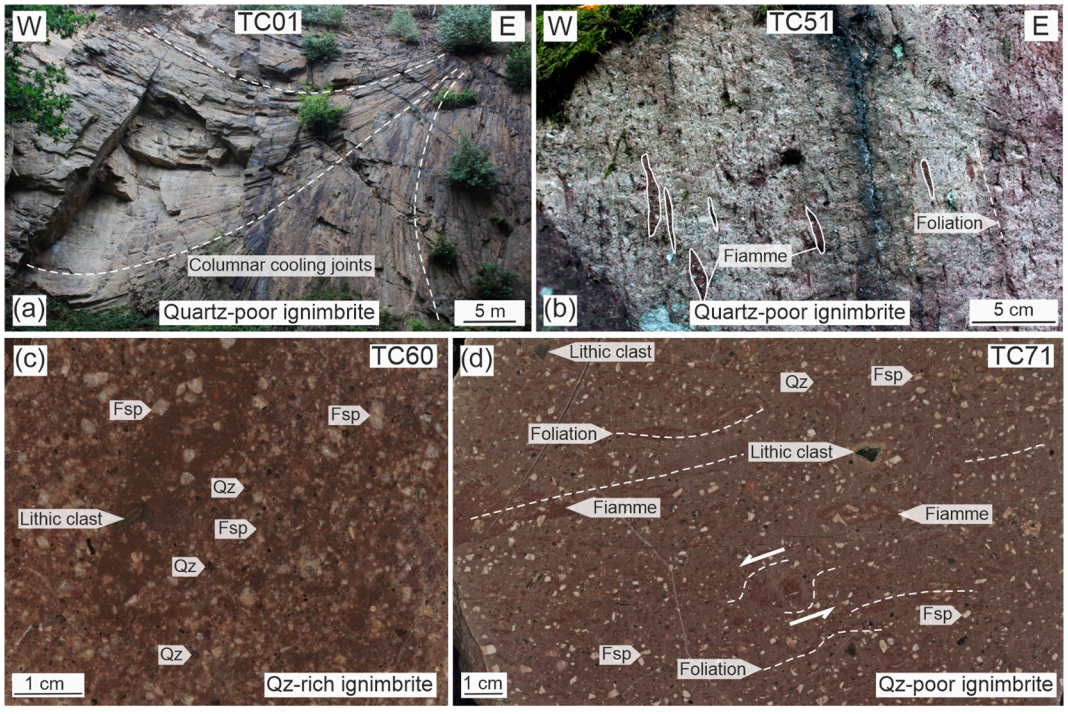

Fig. 2. Close-up view of main ignimbrite lithotypes. (a) Quartz-poor ignimbrite outcrop exposing a fan-like pattern of columnar cooling joints in an abandoned quarry near Grund. (b) An example of flow foliation defined by the preferred orientation of fiamme in a foliation perpendicular section, quartz-poor ignimbrite. Representative photos of rock slabs showing (c) the isotropic texture of quartz-rich ignimbrite, and (d) flow-foliated quartz-poor ignimbrite. Fsp – feldspar, Qz – quartz. See the supplementary material for WGS84 coordinates.

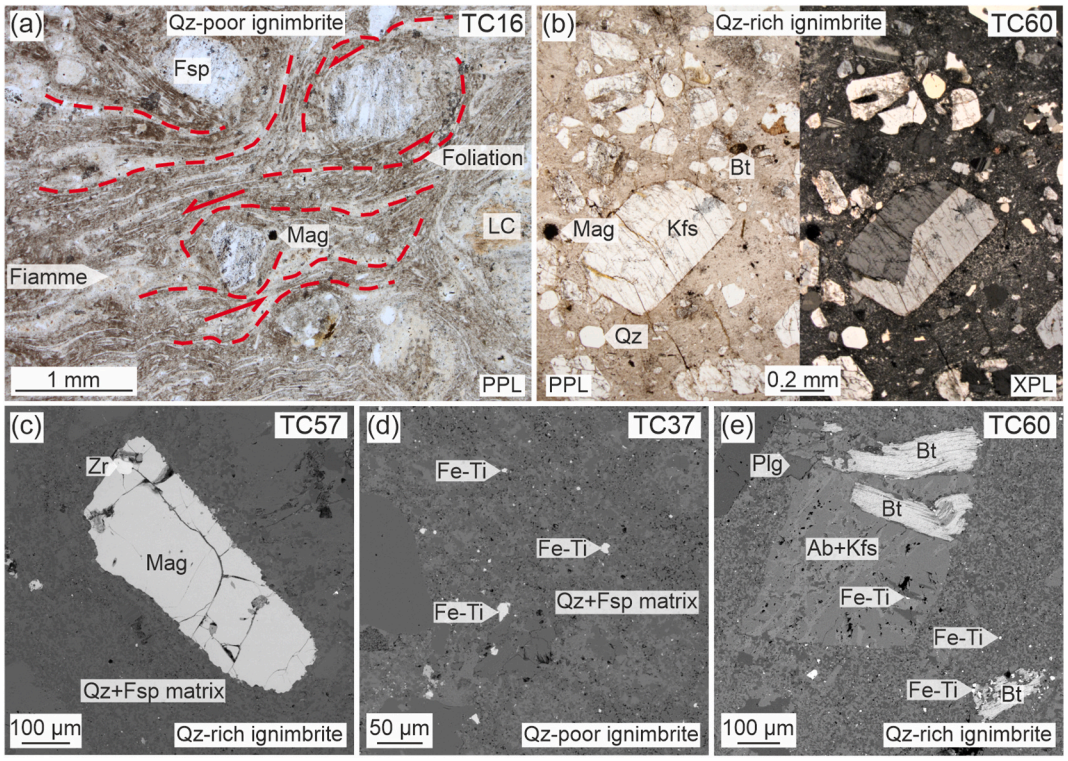

Fig. 3. Microphotographs showing (a) quartz-poor ignimbrite with eutaxitic texture dominated by a fine-grained and recrystallized quartzo-feldspathic matrix hosting elongated devitrified fiamme, feldspar and quartz phenocrysts, accessory magnetite, and lithic clasts. (b) Quartz-rich ignimbrite showing abundant feldspar and quartz phenocrysts, and accessory biotite and magnetite microphenocrysts. Backscattered electron images display (c) a representative of a large and elongated magnetite microphenocryst embedded in a quartzofeldspathic matrix of a quartz-rich ignimbrite; (d) less abundant very fine-grained magnetite grains and aggregates scattered in the matrix of the quartz-poor ignimbrite; and (e) magnetite in form of rims and inclusions in altered biotite and feldspar phenocrysts in quartz-rich ignimbrite. Fsp – feldspar, Ab – albite, Kfs – potassium feldspar, Qz – quartz, Mag – magnetite, LC – lithic clast, Fe–Ti – iron-titanium oxides, Zr – zircon, Bt – biotite; PPL – plain polarized light, XPL – crossed polarized light. See the supplementary material for WGS84 coordinates.

provides other parameters that allow a semi-quantitative correlation with strain (Table 1; Borradaile, 1987, 1991; Borradaile and Jackson, 2010). For the purposes of this manuscript, we use the following parameters: (1) volume normalized bulk (mean) susceptibility (k_m, dimensionless in SI units), (2) degree of anisotropy (P), and (3) shape parameter (T).

The conventional low-field in-phase AMS and recently introduced out-of-phase AMS techniques represent two phases into which the alternating-field AMS signal can be decomposed (Hrouda et al., 2017, 2022). The in-phase magnetic susceptibility (ipk_m) reflects an integrated contribution of all the minerals in the specimen (diamagnetic, paramagnetic, and ferromagnetic). The ipk_m of a rock specimen is strongly dependent on the dominant carrier(s) of the magnetic susceptibility (Tarling and Hrouda, 1993). On the other hand, the out-of-phase magnetic susceptibility (opk_m) reflects only some ferromagnetic minerals such as pyrrhotite, hematite, maghemite, titanomagnetite, and magnetically viscous ultrafine magnetite (Table 1; Jackson et al., 1998; Hrouda et al., 2013, 2018a). The investigation of opAMS, in addition to the ipAMS, can reveal a possible existence of magnetic subfabrics that allow detailed interpretation of emplacement processes (Hrouda et al., 2020; Cruz et al., 2022). The ipAMS and opAMS were measured on an AGCIO KLY5 Kappabridge in the Laboratory of Rock Magnetism, Institute of Geology and Paleontology, Charles University (Prague, Czech Republic).

4.3. Anisotropy of anhysteretic remanent magnetization

The anisotropy of anhysteretic remanent magnetization (AARM) technique was used to separate the contribution of remanence-bearing grains (e.g., magnetite) from the rock matrix and other magnetic fabric. In addition, AARM allows for the evaluation of magnetic subfabrics, and a possible contribution of inverse magnetic fabrics due to the presence of single-domain grains (Rochette, 1988). Furthermore, these data improve a comprehensive interpretation of ipAMS and opAMS magnetic fabric (Table 1; e.g., Rochette et al., 1999; Chadima et al., 2009; Černý et al., 2020; Hrouda et al., 2020). We measured the AARM by imparting a set of directional anhysteretic remanences over the coercivity range of the specimen to obtain the directional variability of the remanent magnetization (e.g., Hrouda, 1982; McCabe 1985; Jackson 1991; Hrouda 2002b; Hrouda et al., 2018b).

The AARM acquisition experiments were performed initially on one specimen from site TC30 to establish the applied field and demagnetization parameters. The maximum measured coercivity window was 20–60 mT and viscosity was 1% expressed by the decrease of magnetization in time. Once these parameters were set, we measured the remaining seventeen sites with the same setup. The natural remanent magnetization (NRM) of each specimen was measured and the NRM was then fully demagnetized in a 120 mT applied field. Specimens were then progressively magnetized in 6 directions with a weak uniaxial DC field of 500 µT and a decaying AC field of 60 mT. The AARM remanence tensors were evaluated using the least-square method. The AARM data were obtained using an AGICO JR-6A spinner magnetometer, LDA5 alternating field demagnetizer, and PAM1 pulse/anhysteretic magnetization unit at the Laboratory of Rock Magnetism, Institute of Geology and Paleontology, Charles University (Prague, Czech Republic).

4.4. Magnetic mineralogy

To identify magnetic minerals carrying the bulk magnetic signal and the relative contribution of paramagnetic and ferromagnetic grains, we

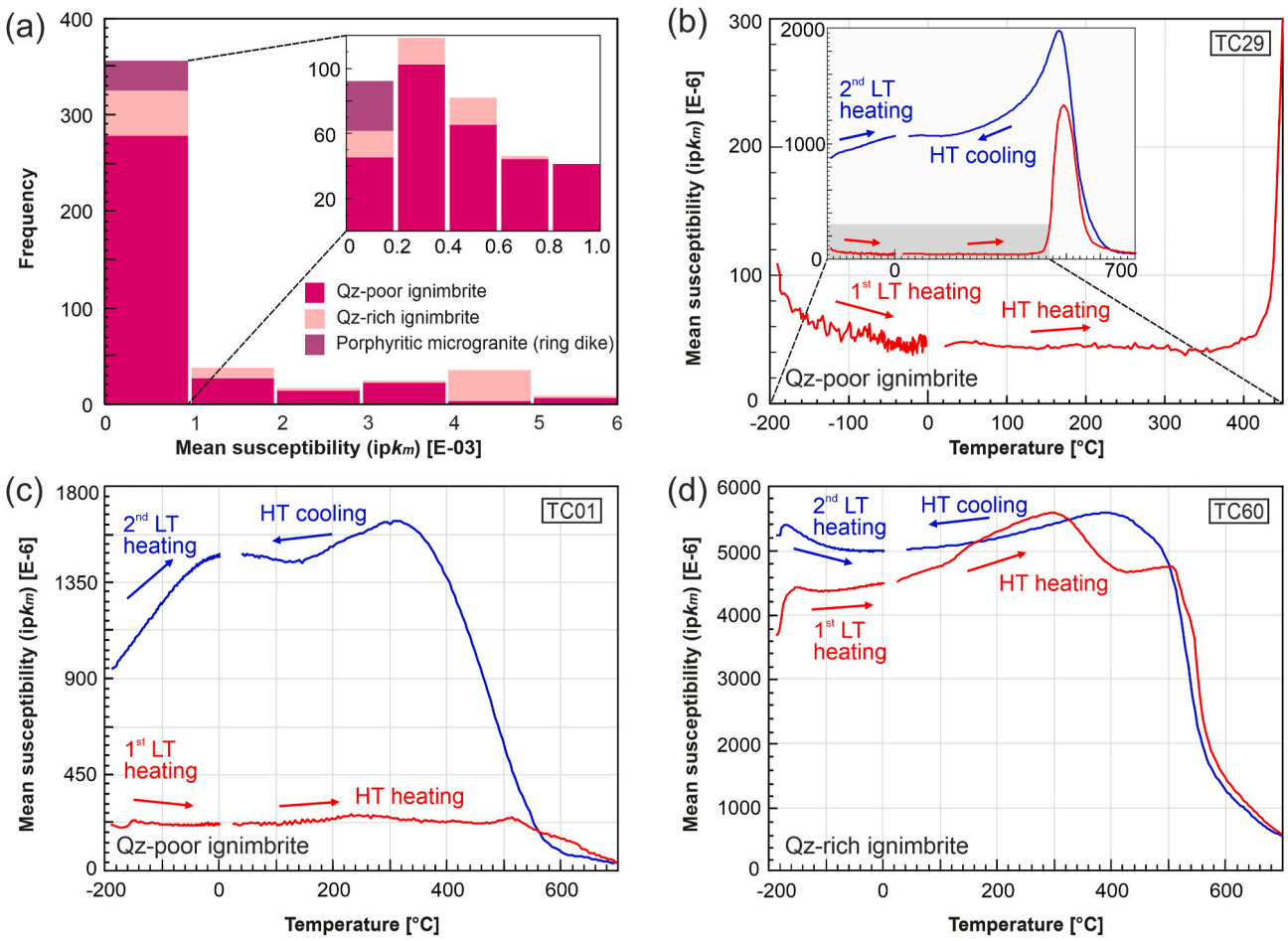

Fig. 4. (a) Histogram showing the distribution of the in-phase susceptibility of all individual specimens. Representative thermomagnetic susceptibility curves of (b) a dominantly paramagnetic specimen with a pronounced hyperbolic shape, the inset shows the full course of the curve TC29 from quartz-poor ignimbrite; (c) specimen of a quartz-poor ignimbrite with a mixture of paramagnetic and ferromagnetic signature; and (d) specimen of a quartz-rich ignimbrite dominated by ferromagnetic magnetite. LT – low temperature, HT – high temperature. See the supplementary material for WGS84 coordinates.

measured thermomagnetic susceptibility curves (k_m–T curves; Orlický, 1990; Hrouda, 1994; Hrouda et al., 1997; Petrovský and Kapička, 2006). The k_m–T curves were obtained by progressive measurement of the bulk susceptibility during the heating of the specimen from ca. −196 °C (boiling temperature of liquid nitrogen) to 5 °C (1st low-temperature heating), heating up from room temperature (ca. 21 °C) to 700 °C (high-temperature heating) and spontaneous cooling back to the room temperature (high-temperature cooling). A second low-temperature measuring cycle was then repeated (2nd low-temperature heating). The repeated cooling, heating, and cooling cycles allow for the characterization of the secondary magnetic phases potentially formed during the experiment. All experiments were conducted in an inert argon atmosphere to minimize oxidation. Powdered specimens were measured using AGICO CS-L Cryostat and CS4 Furnace connected to the KLY5 Kappabridge.

To identify the magnetic domain state(s) we employed magnetic hysteresis loops and first-order reversal curve distribution experiments (Roberts et al., 2000). Magnetic Hysteresis and FORCs were measured on a Lake Shore Cryotronics High performance 8600 Vibrating Sample Magnetometer at the New Mexico Highlands University Paleomagnetic-Rock Magnetic laboratories (NM, USA). Both techniques are used to determine the magnetic mineral domain states and relative composition of the oxides (e.g., Day et al., 1977; Roberts et al., 2022).

The frequency-depended susceptibility (XFD) and normalized frequency-dependent susceptibility (XFN) were used to assist in the mineral identification of the opAMS signal (Table 1; Dearing et al., 1996; Hrouda, 2002b, 2011; Hrouda et al., 2006, 2009; Hrouda and Ježek, 2014). The data obtained from the XFD and XON provide a means to identify ultra-fine grains and viscous magnetic particles. These ultra-fine particles, at times, may carry a different magnetic fabric compared to the bulk AMS fabric of the rock (e.g., Eyre, 1997; Dearing et al., 1996; Hrouda, 2011; Hrouda et al., 2006, 2009; Hrouda and Ježek, 2014). Measurements of frequency-dependent susceptibility and related parameters were obtained at two operation frequencies. The instrument setting was 976 Hz, 200 A/m field intensity for measuring low frequency, and 15.616 Hz, 200 A/m for high-frequency XFD. Measurements were obtained on an AGICO MFK2-FA Kappabridge in the AGICO laboratory, Brno, Czech Republic.

5. Results

5.1. Field observations, structures, and textures

The Qz-poor ignimbrite shows apparent columnar cooling joints with a dominantly steep to subvertical plunge, whereas locally a fan-like structure was observed (Fig. 2a). Only at one site (TC35) located in the peripheral part of the Qz-rich ignimbrite at the present-day erosional level, the moderately-plunging columnar joints were recognized.

The flattened fiammes (up to 8 cm in length) are present in both ignimbrites at the majority of the examined sites, but they are more abundant in the Qz-poor ignimbrite (Fig. 2b and d). The flow foliation defined by the shape-preferred orientation of fiamme measured on

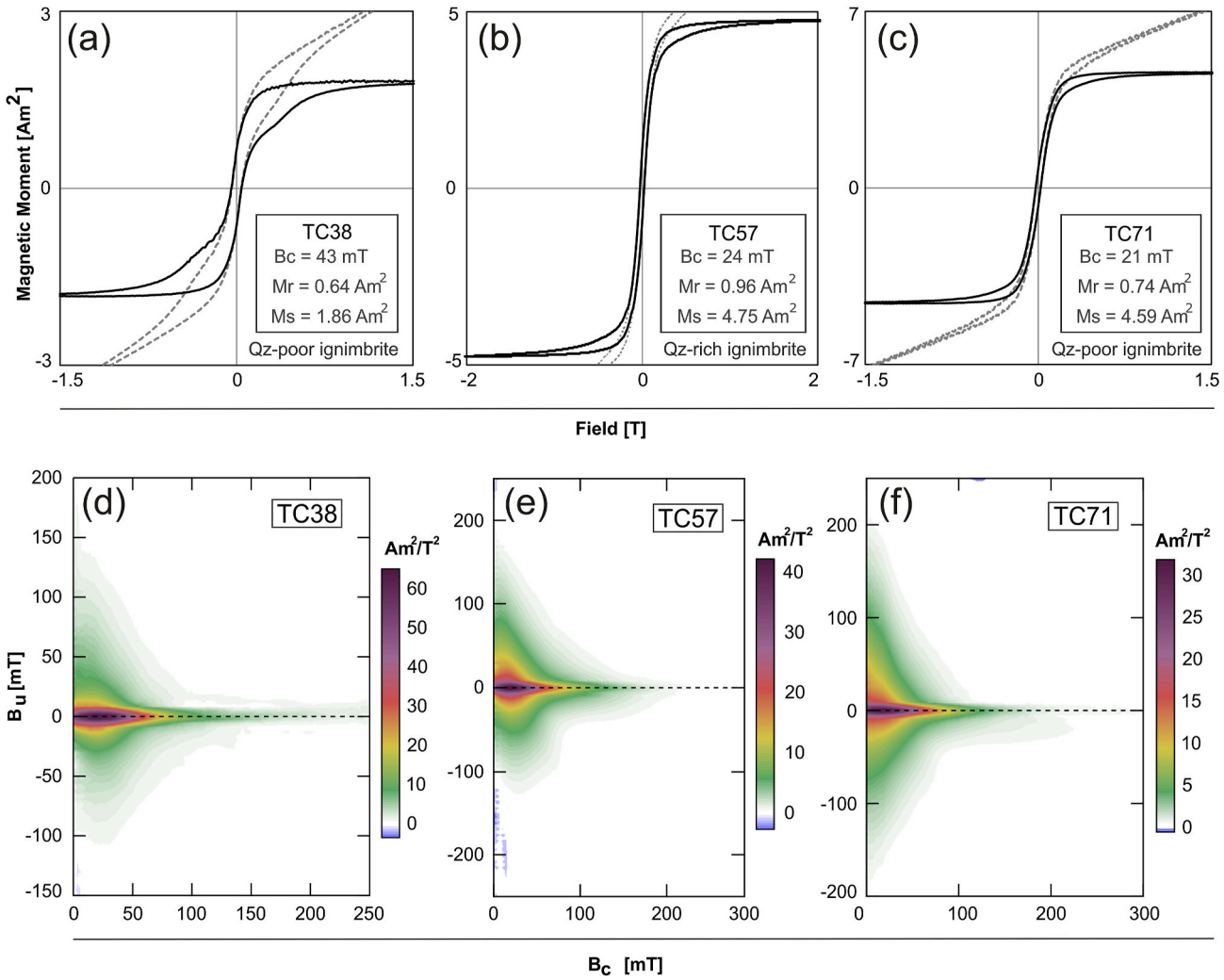

Fig. 5. Representative magnetic hysteresis loops and first-order reversal curves (FORC). (a, b, c) Examples showing the magnetic hysteresis loops of uncorrected (dashed grey lines) and corrected (solid black lines) for paramagnetic signal. Magnetic hysteresis parameters are Bc – field coercivity [mT], Mr – remanent magnetization [Am^2], and Ms – saturation magnetization [Am^2]. (d, e, f) Corresponding FORC distributions were obtained using the following gridded smoothing: vertical ridge – 5; central ridge – 3; horizontal and vertical smoothing: 7; Ba – negative saturation applied field, Bb – positive saturation applied field, Bu = (Ba + Bb)/2. See the supplementary material for WGS84 coordinates.

outcrops and documented by Benek (1980) varies greatly across the entire caldera in terms of both the dip direction and dip. In general, the subhorizontal to subvertical foliations resemble a concentric pattern that mimics the caldera shape. Subhorizontal foliation is present mostly in the central areas and in the southern, southeastern, and northern parts of the caldera, while steep to subvertical and generally inward-dipping foliations occur in the southwestern, northwestern, and northeastern parts of the caldera (Fig. 1). No apparent relationship between the trend and plunge of cooling joints and flow foliation was observed. The porphyritic microgranite ring dike yields subvertical flow foliation defined by the shape-preferred orientation of K-feldspars phenocrysts that is oriented parallel to the dike strike (Fig. 1).

In both lithotypes, the phenocrysts are embedded in a fine-grained matrix composed of a quartz, orthoclase, and plagioclase mixture with a pseudo-fluidal texture (Fig. 3). Apart from quartz phenocrysts, feldspars are dominated by in places sericitized orthoclase. Most phenocrysts are highly fragmented due to the explosive eruption (Fig. 3c). In detail, micro-scale fiammes are present in both the ignimbrite lithotypes and define eutaxitic to parataxitic texture implying a high degree of welding compaction (Fig. 3a and b). Tabular biotite and rare muscovite up to 200 μm long occur as minor accessory minerals, as well as individual microphenocrysts of Fe–Ti oxides scattered throughout the matrix (Fig. 3a–d). Magnetite and rarely also ilmenite form anhedral to euhedral elongated phenocrysts up to 80 μm in Qz-poor ignimbrite and up to 500 μm in Qz-rich ignimbrite (Fig. 3). Fe–Ti oxide grains also form thin rims around feldspar phenocrysts and microinclusions in some sericitized feldspars and biotite (Fig. 3e).

5.2. Magnetic mineralogy

5.2.1. Magnetic susceptibility

The ipk_m values of individual specimens in the Qz-poor ignimbrite range from 39.4×10^{-6} to 5746.3×10^{-6} (with a mean k_m of 859.0×10^{-6}), while most of the values are clustered between 39.4×10^{-6} and 549.4×10^{-6}. The site-mean k_m values indicate 12 ferromagnetic sites with $k_m > 500.0 \times 10^{-6}$ and 12 paramagnetic sites with $k_m < 500.0 \times 10^{-6}$ (Fig. 4a, Table S2). The Qz-rich ignimbrite shows a slightly higher k_m. The susceptibility of all specimens yields a range from 10.6×10^{-6} to 5080.0×10^{-6} with a mean value of 2025.4×10^{-6}. The site-mean values indicate two and four sites with dominant paramagnetic and ferromagnetic susceptibility, respectively. The susceptibility of the porphyritic microgranite ring dike is relatively low ranging from 40.6×10^{-6} to 131.8×10^{-6} with a mean value of 89.6×10^{-6} (Fig. 4a, Table S2). The majority of specimens have a much lower opk_m compared

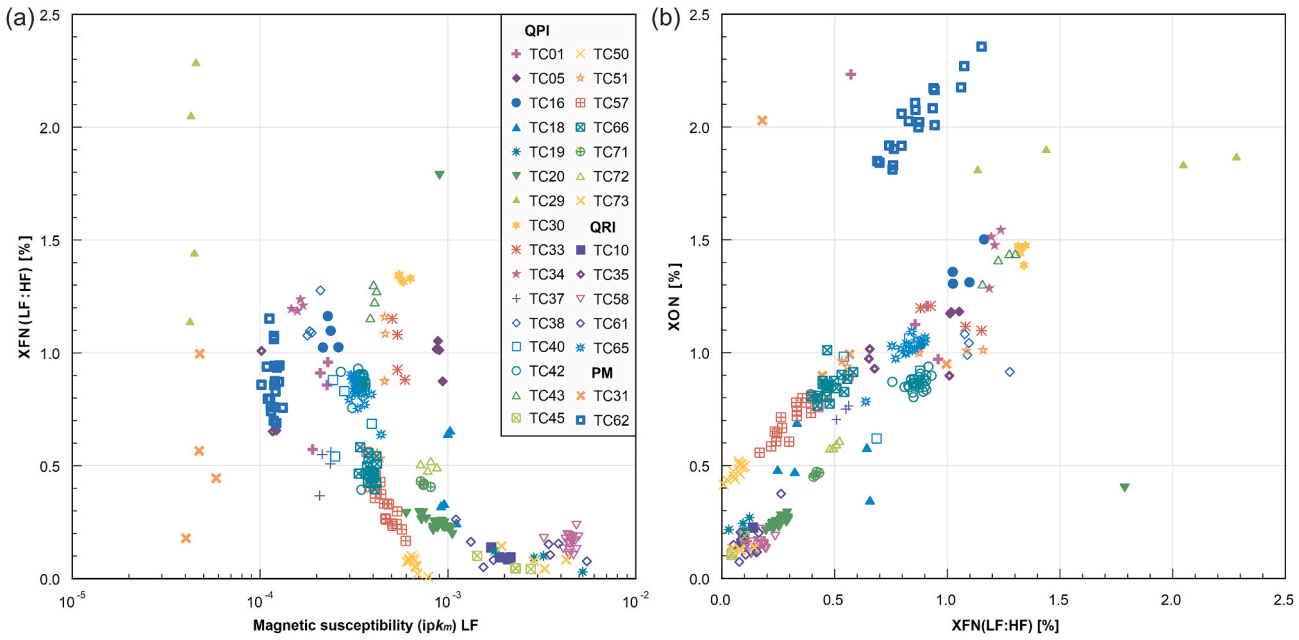

Fig. 6. Frequency-dependent magnetic susceptibility diagrams without the rejected specimens (see the text for details). (a) Diagram showing a relation between the normalized frequency-dependent susceptibility (XFN) and the in-phase magnetic susceptibility (ipk_m) measured at 976 Hz (low frequency; LF). (b) Diagram displaying the relation between XFN, and normalized frequency-dependent susceptibility based on phase angle measured on one frequency (XON). Color-coded symbols represent values from individual sites, see the inset for explanations. See the supplementary material for WGS84 coordinates. (For interpretation of the references to color in this figure legend, the reader is referred to the Web version of this article.)

to ipk_m. The out-of-phase susceptibility ranges by three orders from 10^{-7} to 10^{-5} with a mean value of 5.5×10^{-6}. No spatial distribution pattern of susceptibility is evident in the map view (Fig. S5).

5.2.2. Thermomagnetic susceptibility curves

Three types of k_m–T curves were distinguished based on: (1) the presence of a hyperbolic decrease of susceptibility with increasing temperature in the first low-temperature heating curve (specimens TC29 and TC31); (2) the increase in susceptibility attributed to the Verwey transition at about −150 °C followed by a hyperbolic decrease and later a slight susceptibility increase terminated by a Curie point temperature around 580 °C in the high-temperature heating curve (specimens TC01 and TC35), and (3) a pronounced Verwey transition (ca. −150 °C), followed by a flat course of susceptibility with increasing temperature, which is terminated by an abrupt drop of susceptibility with a Curie point at ~580 °C (specimens TC18, TC30, TC57, TC60, and TC66; Figs. 4d, S3). All specimens have irreversible behavior with a significantly higher susceptibility in the cooling curve and the second low-temperature heating curve, and most specimens also yield a pronounced susceptibility peak between ~420 and 560 °C (Figs. 4b–d, S3). The ferromagnetic specimen TC19 is somewhat different showing a moderate increase in susceptibility from room temperature to ~350 °C followed by a flat pattern until a sharp drop at ~520 °C. The high-temperature cooling curve first roughly follows the heating curve with a subtle Curie point at ~530 °C, which is followed by a steep increase of susceptibility with increasing temperature to ~360 °C. The susceptibility then decreases steadily down to ca. −196 °C (Fig. S3).

5.2.3. Hysteresis loops and FORCs

The magnetic hysteresis results show loops consistent with various magnetic behaviors (i.e., single-domain, vortex state, and multi-domain). Most hysteresis loops are wasp-waisted or goose-necked in shape suggesting that the ignimbrite specimens (both lithotypes) have a mixture of magnetic domain states and/or ferromagnetic minerals (Fig. 5a–c). The FORC diagram displays a range of behavior from vortex state (pseudo-single-domain) to multi-domain state with the presence of non-interacting single-domain particles (Fig. 5d–f). Two specimens from the Qz-rich ignimbrite (i.e., TC35 and TC57; Figs. 5, S4) have similar magnetic behavior (i.e., a mixture of vortex state and single-domain particles).

5.2.4. Frequency-dependent magnetic susceptibility

The XFN parameter of the analyzed specimens is rather low, with values ranging from 0 to 2.3%, and with an average of 0.6%. Most of the values do not exceed 1.4% of dependence. The relatively highest dependence was measured at sites TC29, TC30, TC43, TC34, and TC38 (Fig. 6a and b, Table S2). The XFN increases with decreasing LF susceptibility (Fig. 6a) and increases with the XON parameter (Fig. 6b). A few specimens that yielded XFN values close to zero and negative values (i.e., site TC60), are attributed to measurement noise, and these specimens were excluded from further interpretation of XFN.

5.3. Magnetic fabrics

5.3.1. Degree of anisotropy and shape parameter

The degree of in-phase anisotropy (ipP) of all individual specimens of the Qz-poor ignimbrite ranges from 1.003 to 1.100 (0.3–10% anisotropy) with a mean value of all individual specimens of 3.1%. The shape of the in-phase anisotropy parameter (ipT) ranges from −0.938 to 0.882 and the mean ipT is −0.303. (Fig. 7, Table S2). The Qz-rich ignimbrite yields the ipP parameter from 1.005 to 1.104 (0.6–10.4% of anisotropy) and the mean value is 3.1%. The range of ipT values is from −0.852 to 0.887, while the mean value is −0.073 (Fig. 7). The ipP from the ring dike specimens is significantly lower with a mean value of 1.008 and the ipT mean value is 0.267 (Fig. 7).

The out-of-phase degree of anisotropy (opP) of all specimens is relatively higher as compared to ipP, ranging from 1.013 to 2.948 (1.1–294.8% anisotropy) with a mean value of 1.114 (11.4%), which is significantly higher than ipP (Fig. 7). The in-phase and out-of-phase shape parameters (ipT and opT) then show similar behavior. The opT of all individual specimens ranges from −0.910 to 0.962, and the mean value is −0.062 (Fig. 7). All the parameters do not show any trend in

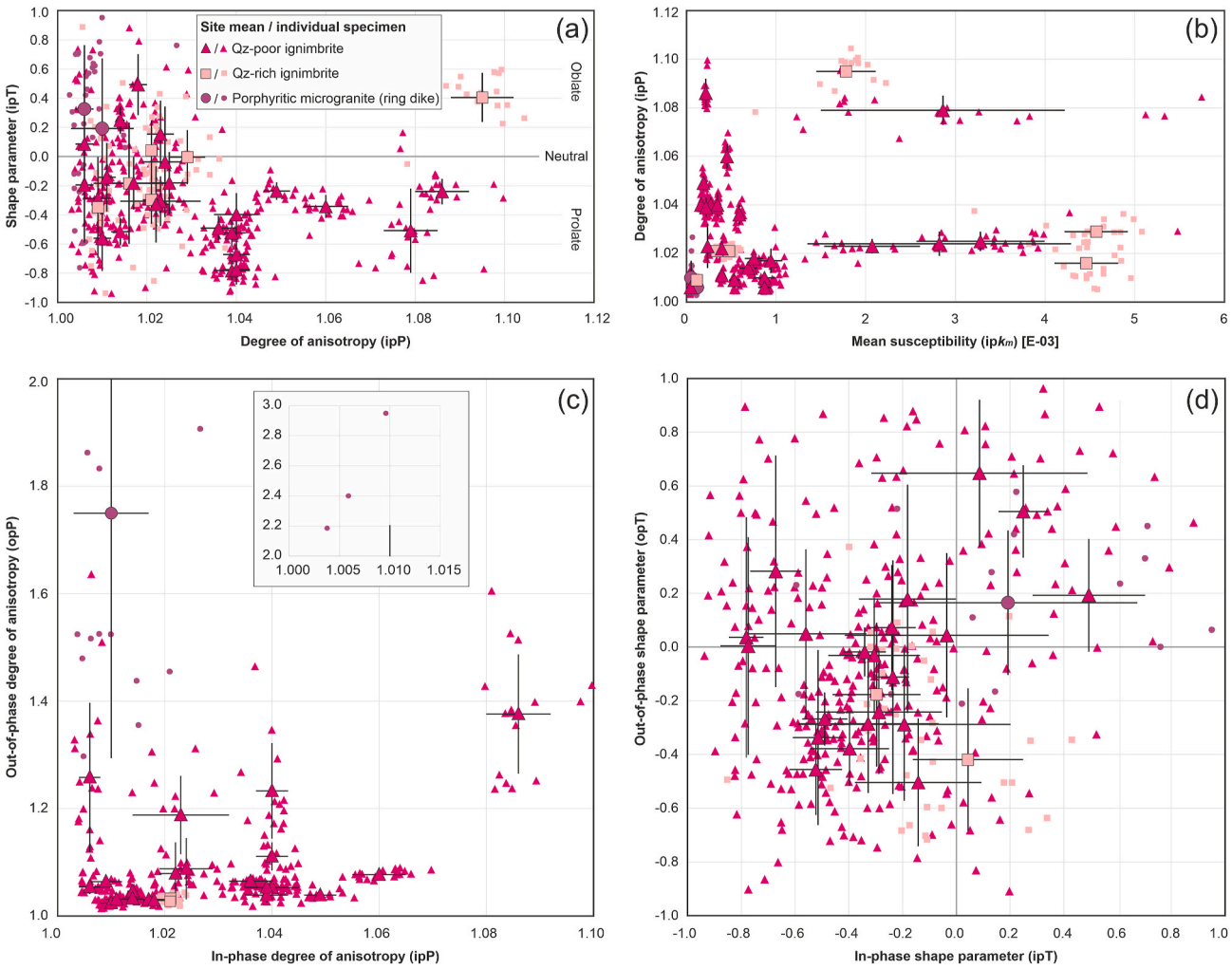

Fig. 7. Diagrams showing the relations of AMS parameters for in-phase and out-of-phase susceptibility. Rejected specimens are not displayed (see the text for details). (a) Degree of anisotropy versus shape parameter of ipAMS. (b) Mean (bulk) susceptibility versus degree of anisotropy of ipAMS. (c) In-phase versus out-of-phase degree of anisotropy. The inset diagram shows three data outliers. (d) In-phase versus out-of-phase shape parameter. The error bar is the standard error of the mean.

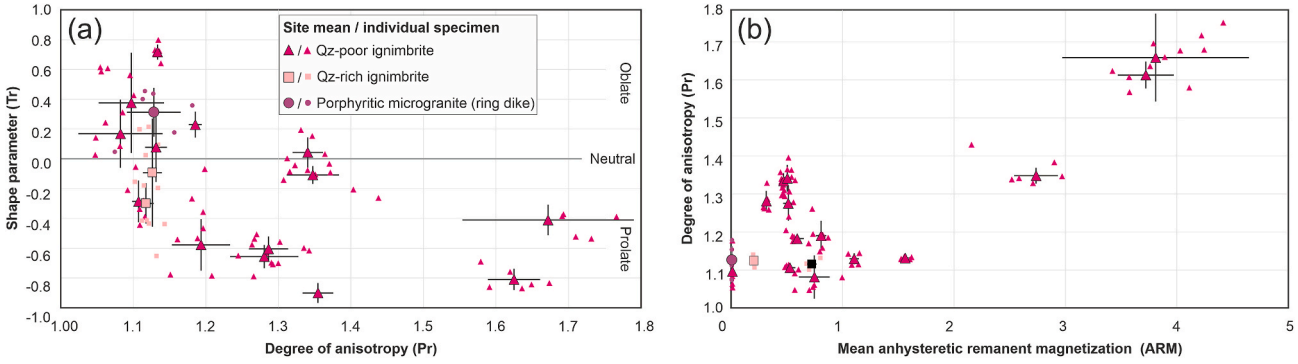

Fig. 8. Diagrams showing the relations of AARM parameters. (a) Degree of anisotropy (Pr) versus shape parameter (Tr). (b) Mean ARM versus degree of anisotropy (Pr). The error bar is the standard error of the mean.

their spatial distribution on the map (Fig. S5).

5.3.2. *Reliability and precision of magnetic fabric*

The ipAMS of individual specimens indicates relatively high values of F-statistics (on average: F = 211,977.88, F_{12} = 34,339.75, F_{23} = 14,554.32; after Jelínek, 1978) and low confidence semi-axes angles around the eigenvectors (on average: $e_{12} = 3.07$, $e_{23} = 3.21$, $e_{13} = 1.03$), implying a well-defined anisotropy. Exceptions are sites TC29, TC31, TC35, and TC62 with larger confidence ellipses of individual specimens and a rather poor clustering of principal susceptibility axes (K_1, K_2, and K_3) round their mean value due to very low susceptibility and low degree of anisotropy. These sites are analyzed further with caution.

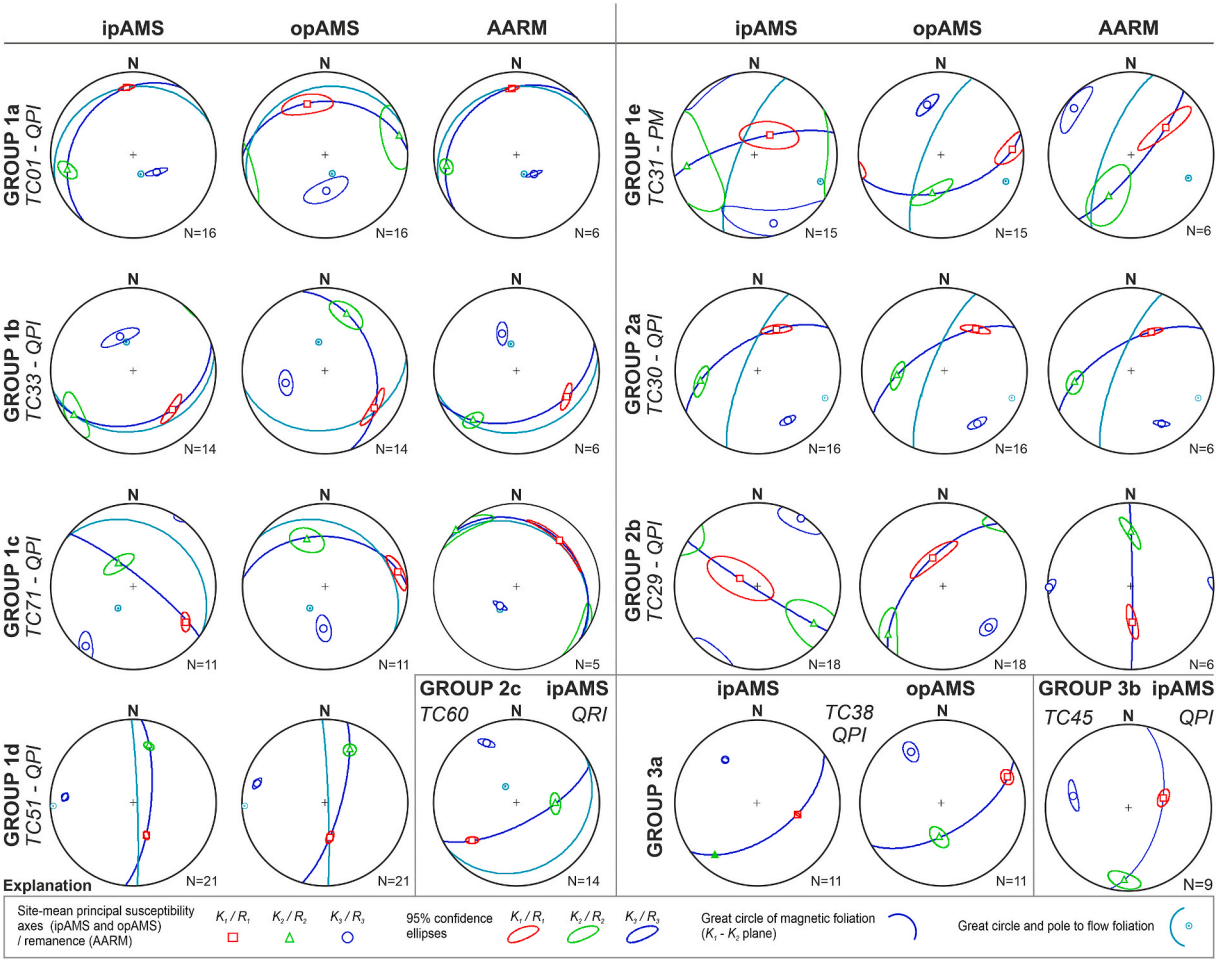

Fig. 9. Representative stereonets of magnetic multi-fabrics obtained by ipAMS, opAMS, and AARM. Each diagram shows mean orientations of principal susceptibility/remanence axes and their confidence ellipses at the site level. Flow foliation planes are also reported as cyan great circles and poles to planes. QPI – Quartz-poor ignimbrite, QRI – Quartz-rich ignimbrite, PM – porphyritic microgranite ring dike. Stereograms of all measured sites are displayed in Supplementary Material Fig. S6. The full dataset is provided in Table S2. (For interpretation of the references to color in this figure legend, the reader is referred to the Web version of this article.)

Most of the sites yield clustered principal susceptibility axes K_1, K_2, and K_3 of individual specimens around their mean values. For the purpose of this manuscript, we informally define the threshold value for well-clustered susceptibility axes as those with confidence estimates less than 30° about the mean based on the major semi-axis of the confidence ellipse of mean susceptibility tensor after Jelínek (1978) (Table S2). The sites with more dispersed individual specimens and confidence ellipses greater than 30° (TC19, TC29, TC31, TC35, TC61, and TC62), were analyzed with caution.

On average, the opAMS of individual specimens indicates up to three orders of magnitude lower values of F-tests values (on average: $F = 535.18$, $F_{12} = 86.53$, $F_{23} = 35.32$) and one order higher confidence ellipses semi-axis angles around the eigenvectors compared to the ipAMS (on average: $e_{12} = 26.73$, $e_{23} = 27.13$, $e_{13} = 9.32$), indicating a lower but still defined anisotropy. Sites TC35 and TC62 have significantly low F-tests and high confidence ellipses, respectively. Sites TC10, TC19, TC45, TC58, TC60, and TC73 yield either close to zero or negative opk_m and/or poorly constrained anisotropy. This behavior is attributed to an artifact of susceptibility signal decomposition. Thus, these sites were excluded from further magnetic fabric interpretation.

For the remaining sites, the out-of-phase principal susceptibility axes K_1, K_2, and K_3 are relatively well clustered with respect to the mean value in most cases (Fig. S6). Five sites, with confidence estimates greater than 30°, (TC16, TC34, TC40, TC61, and TC62) were also analyzed with caution. The mean values of the degree of anisotropy and shape parameter (both the in-phase and out-of-phase) are independent of the clustering/dispersion of principal susceptibilities of individual specimens around their mean values.

5.4. Anisotropy of anhysteretic remanent magnetization

The anhysteretic remanent magnetization (ARM; Hrouda, 2002a) of all individual specimens ranges from 5.66×10^{-3} to 4.42×10^{0} [A/m], with most of the values clustered between 5.66×10^{-3} and 8.96×10^{-1} [A/m], while sites TC43, TC30, and TC33 have significantly higher site-mean ARM of 2.74×10^{0}, 3.72×10^{0} and 3.81×10^{0} [A/m] (Table S2). The degree of anisotropy (Pr) of all specimens spans from 1.048 to 1.766 (4.8%–76.6% anisotropy) with a mean value of 25%. The shape parameter (Tr) ranges from −0.972 to 0.797, and the mean value is −0.163, with the majority of specimens plotting in the prolate field. (Fig. 8a). The Pr parameter is relatively higher as compared to ipP and opP (3.1% and 11.4% respectively; Figs. 7 and 8). We observe a trend of increasing Pr with increasing ARM. Specimens with low Pr show a spectrum of Tr parameters from oblate to prolate, whereas the higher anisotropic specimens reveal only prolate shapes of the AARM ellipsoid (Fig. 8). The ARM, degree of anisotropy, and shape parameter show a rather random distribution on the map (Fig. S5). Out of 17 sites, 11 sites are well-clustered based on R_1, R_2, and R_3 confidence ellipses of the mean tensors. The remaining sites (TC19, TC20, TC31, TC34, TC43, and TC71) were further analyzed with caution.

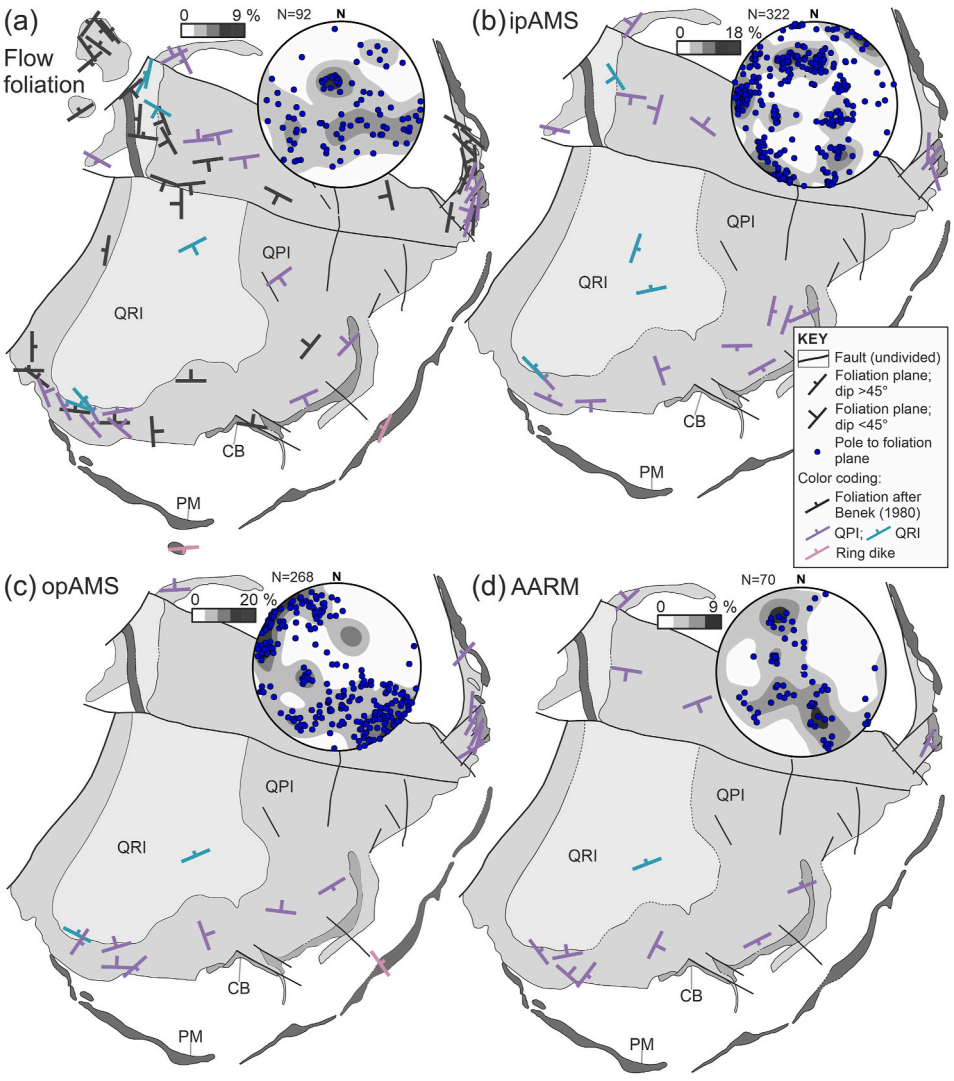

Fig. 10. Simplified maps of the TWC showing dip direction and dip symbols of (a) flow foliations; (b) ipAMS foliations; (c) opAMS foliations; and (d) AARM foliations. Symbols of poles to the foliation planes are also plotted on an equal area, lower hemisphere stereographic projections. The rejected data are not displayed (see the text for details). QPI – Quartz-poor ignimbrite, QRI – Quartz-rich ignimbrite, PM – porphyritic microgranite ring dike, CB – collapse breccia (monolithic gneiss mesobreccia with a pyroclastic matrix). Maps are based on Fig. 1. Kamb contours are in standard deviations.

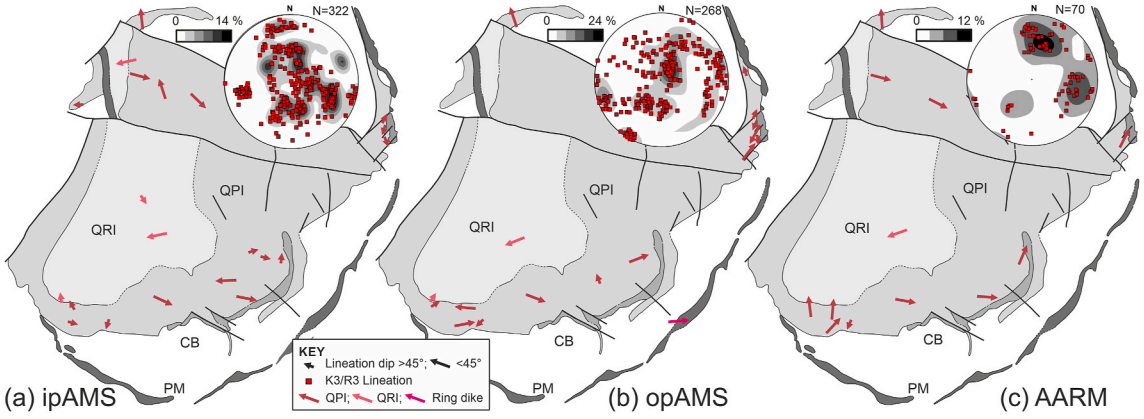

Fig. 11. Simplified maps of the TWC showing trend and plunge symbols of (a) ipAMS lineations; (b) opAMS lineations; and (c) AARM lineations. Magnetic lineations are also plotted on an equal area, lower hemisphere stereographic projections. The rejected data are not displayed (see the text for details). QPI – Quartz-poor ignimbrite, QRI – Quartz-rich ignimbrite, PM – porphyritic microgranite ring dike, CB – collapse breccia (monolithic gneiss mesobreccia with a pyroclastic matrix). Maps are based on Fig. 1. Kamb contours are in standard deviations.

Table 1
Rock-magnetic parameters used in this manuscript.

Parameter	Explanation	Mathematical expression	References
Anisotropy of In-phase (ip) and out-of-phase (op) magnetic susceptibility (AMS)			
k_m	bulk (mean) susceptibility	$(K_1 + K_2 + K_3)/3$	Nagata (1961)
K_1, K_2, K_3	principal susceptibilities	$K_1 \geq K_2 \geq K_3$	Nye (1957)
K_1–K_2	magnetic foliation plane		
K_1	magnetic lineation		
P	degree of anisotropy	K_1/K_3	Nagata (1961)
T	shape parameter	$2ln\ (K_2/K_3)/ln\ (K_1/K_3) -1$	Jelínek (1981)
Anisotropy of anhysteretic remanent magnetization (AARM)			
ARM	anhysteretic remanent magnetization	$(R_1 + R_2 + R_3)/3$	After Jackson (1991) and Hrouda (2002a)
R_1, R_2, R_3	principal anhysteretic remanent magnetizations	$R_1 \geq R_2 \geq R_3$	After Nye (1957)
R_1 - R_2	magnetic foliation plane		
R_1	magnetic lineation		
Pr	degree of anisotropy	R_1/R_3	After Nagata (1961) and Jackson (1991)
Tr	shape parameter	$2ln\ (R_2/R_3)/ln\ (R_1/R_3) -1$	After Jelínek (1981)
Frequency-dependent susceptibility			
XFD	frequency-dependent susceptibility	$100 \times (kLF–kHF)/kLF\ [\%]$	Dearing et al. (1996)
XFN	normalized frequency-dependent susceptibility	$XFD/(lnHF - lnLF)$ [%]	Hrouda (2011)
XON	normalized frequency-dependent susceptibility	$(200/\pi) \times tan\delta$	Hrouda et al. (2013)
δ	phase angle	$tan\delta = X''/X'$	Hrouda et al. (2013)

kLF - in-phase susceptibility at LF; *kHF* - in-phase susceptibility at *HF*; *LF* - low frequency (976 Hz), *HF* - high frequency (15,616 Hz); *X''* - out-of-phase susceptibility; *X'* - in-phase susceptibility.

6. Interpretation of rock-magnetic dataset

6.1. Source of susceptibility and remanence signal

Rock magnetic mineralogical experiments revealed a variable mixture of paramagnetic and ferromagnetic minerals as carriers of the in-phase magnetic susceptibility. Essentially, even specimens with the lowest susceptibility (i.e., site TC29, $ipk_m = 46.06 \times 10^{-6}$; TC38, $ipk_m = 189.70 \times 10^{-6}$) yield a stable out-of-phase magnetic susceptibility and ferromagnetic remanence behavior (Section 5.2). Hence, we interpret the first two types of thermomagnetic curves (Section 5.2.2) as dominated by paramagnetic (ferro)silicates with a subtle contribution of low-Ti magnetite (Rochette, 1987; Hrouda and Jelínek, 1990), while some new higher-susceptibility mineral phases grew during the heating experiment (Muxworthy and Mcclelland, 2000). The magnetic fabric record is thus a result of the dominant magnetocrystalline anisotropy of biotite and muscovite along with a minor contribution from ferromagnetic phases (Richter et al., 1993; Martín-Hernández and Hirt, 2003).

The third type of thermomagnetic curves shows apparent Verwey transitions and Currie temperatures that imply a dominance of low-Ti titanomagnetite over the paramagnetic mineral phases. Based on the thin-section analysis, the magnetite grains occur dominantly as largely spaced and unequal large grains, while only a few small magnetite grains and clusters of small grains were identified. We interpret the fabric patterns to reflect the shape anisotropy of large magnetite grains, whereas the effect of distribution anisotropy (grain-to-grain magnetic interactions) is negligible given the large spacing of the magnetite grains (see Section 5.1; Hargraves et al., 1991; Stephenson, 1994; Cañón-Tapia, 1996; Harrison and Feinberg, 2009). In addition, the shape of the hysteresis loops and FORCs distribution indicate a mixture of single-domain, vortex state, and multi-domain magnetic behaviors. (Roberts et al., 1995, 2000). The larger and dominant multi-domain magnetites are indicative of 'normal' magnetic fabrics (Rochette et al., 1999; Ferré, 2002; Chadima et al., 2009). Nevertheless, the presence of 'intermediate' or 'inverse' fabrics cannot be conclusively refuted, especially in the presence of some single-domain and vortex state grains. The presence of minor amounts of very fine-grained Fe–Ti oxides (likely single-domain to superparamagnetic) observed along some altered biotite crystals and in the form of inclusions in feldspar phenocrysts may contribute to a composite AMS fabric (Housen et al., 1993; Borradaile and Gauthier, 2003). Bumps around 250–300 °C on some thermomagnetic curves of the ferromagnetic specimens and their irreversible behavior suggest the presence of some coarse-grained titanomaghemite due to deuteric oxidation and/or syn-to post-emplacement hydrothermal alteration (Ade-Hall et al., 1971; Dunlop and Özdemir, 1997; Gee et al., 2010; Petronis et al., 2011).

Frequency-dependent susceptibility revealed that the specimens have a low-frequency dependence typically up to about 1.4%. There is a direct correlation between XON and XFN parameters (Fig. 7), which indicates the presence of a small fraction of magnetically viscous, ultrafine magnetic grains. Their magnetic state is near the transition from a superparamagnetic to a single-domain state (Worm, 1998; Shcherbakov and Fabian, 2005). Hence, the opkm and opAMS are carried by frequency-dependent ultrafine particles. In addition, based on the ARM acquisition test, the AARM signal is carried by a soft magnetite fraction with a small amount of viscous component (Machac et al., 2007).

6.2. Comparison of magnetic fabrics methods

We define three groups of magnetic fabrics in the TWC. These groups are defined based on the relationships between the principal susceptibility (ipAMS and opAMS) and the remanence (AARM) axes, and the orientation of flow and magnetic foliation planes (Figs. 9, S6, Table 2). In all cases, we also present subgroups of magnetic fabric behavior based on a detailed complexities of fabric orientations at a site-scale. Their significance for geologic interpretations is then discussed below.

(1) Group 1 includes 22 sites divided here in five subgoups. (a) Seven sites are characterized by subcoaxial principal axes determined by all applied methods (ipAMS, opAMS in all cases, and AARM in four cases), and parallel flow (if available) and magnetic foliations (sites TC01, TC50, TC57, TC61, TC65, TC73, and TC74). Subgroup (b) comprises sites with similarly oriented ipAMS and AARM axes, and flow foliation (if available) is parallel with

Table 2
Fabric groups in the Tharandter Wald Caldera.

Group		Mutual relations	N
Group 1	a	ipAMS, opAMS, and AARM foliations (sub)parallel with flow foliation*	7
	b	ipAMS and AARM foliations (sub)parallel with flow foliation*; opAMS foliations at high angle	6
	c	opAMS, AARM, and flow* foliations (sub)parallel; ipAMS foliations at high angle	4
	d	ipAMS foliations parallel with flow foliation; opAMS* foliations parallel or at high angle; no AARM data	4
	e	AARM and flow foliation parallel, opAMS and ipAMS foliations at high angle	1
Group 2	a	ipAMS, opAMS, and AARM* foliations (sub)parallel; flow foliation at high angle	2
	b	ipAMS, opAMS, and AARM* foliations at high angle; flow foliation* at high angle	3
	c	ipAMS foliations and flow foliation at high angle; no opAMS and AARM data	2
Group 3	a	ipAMS, opAMS, and AARM foliations at high angle; no flow foliation	1
	b	only ipAMS available	2

N = number of sampling sites; * if available or accepted

ipAMS and AARM magnetic foliations, while the opAMS fabric is discordant (TC05, TC18, TC33, TC34, TC37, and TC40). (c) Sites TC20, TC43, TC71, and TC72 have parallel opAMS, AARM, and flow foliation (if available), while ipAMS is at an angle. The subgroup (d) includes four cases with either ipAMS or opAMS magnetic foliation parallel with flow foliation, while no AARM data are available. Out of these sites, TC42 and TC51 have coaxial ipAMS and opAMS axes, TC16 has non-coaxial ipAMS and opAMS axes, or opAMS was rejected in the case of site TC10. (e) In the case of station TC31, the AARM and flow foliation are subparallel, whereas ipAMS and opAMS foliations are at a high angle.

(2) Group 2 comprises a mixture of 6 sites which yields a different orientation of flow and magnetic foliations. Out of these, subgroup (a) includes sites TC30 and TC66 with subcoaxial principal susceptibility and remanence axes (if available). (b) Sites TC19, TC29, and TC35, yielded non-coaxial axes of each method. (c) Sites TC60 and TC62 yield only ipAMS data and magmatic foliations at a high angle.

(3) Group 3 includes 3 sites where no flow foliation was measured. (a) At site TC38, the ipAMS and opAMS have non-coaxial principal susceptibility axes, and (b) at sites TC45 and TC58, we have only ipAMS data available.

The relation of the examined caldera lithologies and groups of magnetic fabrics as defined above are as follows. Group 1 is dominated by Qz-poor ignimbrite (18 sites, 82%), followed by three sites of Qz-poor ignimbrite and one site of porphyritic microgranite (ring dike). In comparison, Group 2 includes 4 sites of Qz-poor ignimbrite, 2 sites of Qz-rich ignimbrite, and 1 site of porphyritic microgranite. Group 3 has 2 sites of Qz-rich ignimbrite and 1 site of porphyritic microgranite. In other words, Group 1 dominates most of the examined sites, whereas the sites of Groups 2 and 3 are scattered rather randomly across the caldera.

7. Discussion

7.1. Significance and applicability of magnetics fabrics

The well-defined magnetic fabrics of Group 1 are considered reliable for geodynamic interpretations for the following reasons. The general (sub)coaxial pattern of the magnetic fabric axes implies an organized crystallographic anisotropy of micas, shape anisotropy of viscous ferromagnetic minerals (i.e., ultrafine magnetite at the superparamagnetic/single-domain boundary), shape anisotropy of vortex state and multi-domain magnetite, and planar shape preferred orientation of fiamme.

However, there are a few complexities related to individual subroups of Group 1. The pattern of coaxial opAMS and AARM principal axes in Group 1c, which are at a high angle to ipAMS axes, imply that the ipAMS is a combination of two non-coaxial subfabrics carried by paramagnetic ferrosilicates and magnetite fractions entitled as composite or anomalous fabrics (e.g., Housen et al., 1993; Borradaile and Gauthier, 2003). Given that the opAMS and AARM foliation yield fabrics parallel with the flow foliation, we do not attempt to further interpret the composite ipAMS fabrics at these sites.

The different orientations of opAMS axes as compared to ipAMS and AARM in Group 1b, 1d, and 1e are interpreted to reflect a weak and near-random subfabric carried by a small fraction of ultrafine magnetite grains. These grains likely developed during post-emplacement processes, and/or as relics of larger magnetite microphenocrysts that decomposed during hydrothermal alteration (e.g., Nédélec et al., 2015). We assume that the opAMS fabrics in these cases reflect an unorganized late-stage or secondary post-emplacement magnetic fabric, thus opAMS fabrics at these sites provide no relevant structural insights for the flow and emplacement processes of TWC ignimbrites.

Group 2a yields magnetic fabrics (ipAMS, opAMS, and AARM) that are at a high angle to the macroscopic ignimbrite flow fabric. The non-parallel magnetic fabrics of Group 2b and 2c are arguably attributed to a mixture of variable magnetic domain states (multi-domain, vortex state, single-domain, and ultra-fine magnetite) and their fraction. We note that these sites do not yield a readily interpretable fabric pattern. As such, the non-parallel ipAMS, opAMS, and AARM fabrics likely are a result of various effects including the superposition of inverse and composite magnetic fabrics (e.g., Rochette et al., 1999; Borradaile and Jackson 2004, 2010) and hydrothermal alteration (e.g., Nédélec et al., 2015), or their combination. It is worth mentioning that these effects may had different stages in the relative timing of formation likely restricted to post-emplacement processes, as they partially or completely obscure the primary emplacement-related fabric record. For instance, the hydrothermal alteration may lead to a decrease in the magnetic susceptibility and the growth of ARM-bearing iron oxides with fabrics at an angle to the primary emplacement fabric (Group 2b). Although the absolute timing of such alteration is unclear, it may have occurred shortly after ignimbrite emplacement in response to the activity of the underlying magmatic system or could have occurred continuously from the cooling of the source magma chamber(s). Alternatively, fluid mobilization may also be associated with much later faulting.

A late-stage hydrothermal alteration phase(s) that accompanies the volcano plumbing systems is commonly observed at many ancient to recent felsic calderas and may remain active long after caldera collapse (Schirnick et al., 1999; Lindsay et al., 2001; Lipman, 2007; Soler et al., 2007). The effect of alteration on the primary susceptibility-bearing minerals was examined in detail by LaBerge et al. (2009) who pointed out the formation of secondary fabrics defined by the growth of microlites and vapor-phase minerals in pore space during ignimbrite cooling. Schlinger et al. (1988) proposed that microcrystals of magnetite may also nucleate and grow from volcanic glass at high temperatures just after the emplacement. Wang et al. (2001) suggested that steep to vertical magnetic fabrics in ignimbrite deposits may be the result of secondary oxide growth on brittle fractures and columnar jointing that developed after the emplacement. In addition, the later faulting of the TWC along the Grund, Herndorf, Mid-Saxony, and other minor faults may have facilitated hydrothermal circulation, which could potentially alter the rock-magnetic mineralogy (Just et al., 2004; Kontny and Dietze, 2014). Therefore, the magnetic fabrics in Group 2 were rejected from further geological interpretations of caldera emplacement dynamics.

Lastly, taking into the account that ipAMS method was successfully applied to Paleozoic ignimbrites (e.g., Wang et al., 2001; Willcock et al., 2015), we consider the ipAMS data of the Group 3 reliable even without the proxy of other magnetic methods and macroscopic flow foliations. We note, however, that we interpret their geological significance cautiously, but the possible existence of composite magnetic fabrics or the effect of alteration at these sites cannot be conclusively ruled out.

7.2. Emplacement dynamics of TWC ignimbrites

We mapped the overall fabric geometry based on the macroscopic flow foliations (Fig. 10a) and multiple magnetic fabrics (Figs. 10 and 11). In map view, the magnetic foliation planes of the multiple magnetic methods (excluding the rejected data, see details in sections 5.3 and 7.1) define a concentric pattern delineating the overall shape of the TWC (Fig. 10). The sites located close to the inferred caldera margin (in places highlighted by porphyritic microgranite ring dikes) yield rather steep to subvertical foliations dipping generally towards the caldera interior. These foliations are mostly accompanied by steep lineations. Only the AARM data reveal moderately plunging magnetic lineations. At some sites, however, the lineations also show various trends and plunges. Sites located roughly in the caldera interior yield subhorizontal to moderately dipping foliations and lineations (Figs. 10 and 11). The magnetic fabrics of all three methods are also defined by dominantly prolate-shaped ellipsoids.

Such a fabric pattern of an ignimbrite deposit is rather unusual.

Numerous studies report shallowly dipping magnetic foliations that are parallel with macroscopic fabric with the associated magnetic lineation coaxial or perpendicular to the dip direction and dominantly oblate shape of the fabric ellipsoid (Fig. 12a). This type of fabric relationship is referred to as normal magnetic fabric. The acute angle between flow foliation and basal planes is commonly interpreted as representing imbrication that depends on the PDC regime and flow directions (see for instance Fisher et al., 1993; Ort et al., 2003; Giordano et al., 2008; Gountié Dedzo et al., 2011; Agrò et al., 2015 among many others).

Given that flow and magnetic fabrics for the TWC ignimbrites do not reflect typical emplacement geometry for an ignimbrite. In addition, considering that no information on the character of the bedrock paleotopography is available, our dataset does not allow us to directly interpret the pyroclastic flow directions, but additional post-emplacement processes must be considered. The steep to subvertical foliations and prolate character of fabric ellipsoid that dominate the TWC ignimbrites may suggest (1) regional tectonic overprint; (2) alteration of the magnetic mineral phase(s); (3) a fabric controlled by paleotopography, aerial restricted flow confined within the caldera, and/or interaction with hot pyroclastics; (4) welding and/or rheomorphic flow (Ellwood, 1982; Lamarche and Froggatt, 1993; Borradaile and Werner, 1994; Le Pennec et al., 1998; Wang et al., 2001; Pioli et al., 2008; Geissman et al., 2010).

The tectonic overprint can be ruled out as no systematic fabric pattern discordant to the caldera margins that would reflect a regional tectonic strain pattern was observed and the degree of anisotropy is low compared to other tectonically strained rocks. We did not consider rocks that showed evidence of alteration and we rejected sites with suspicious magnetic fabric data. Paleotopography could affect the preserved orientation of magnetic fabric in the lower part of the deposit, however, the upper parts of the ignimbrite sequence should preserve an internally consistent fabric pattern. Finally, most of the petrographic evidence presented by Benek (1980), Breitkreuz et al. (2021), and this study imply that the ignimbrites experienced a high degree of welding and rheomorphism. We thus interpret the fabric pattern of the TWC ignimbrites as follows.

The high-energy caldera-forming eruptions sourced the pyroclastic flows, from which the ignimbrites were deposited on the pre-caldera topography (Fig. 12a). The pyroclastic flows filled paleovalleys and depressions and then formed an extensive ignimbrite sheet, typical for such eruptions (Lipman, 2007). The proximal part of the ignimbrite sheet, now preserved as intra-caldera deposits of the TWC, experienced a chaotic turbulent flow as reflected by the scatter of some of the magnetic lineation (Baer et al., 1997; Paquereau-Lebti et al., 2008). During or shortly after deposition, the ignimbrite deposit while still at high temperatures was strongly welded and likely underwent local

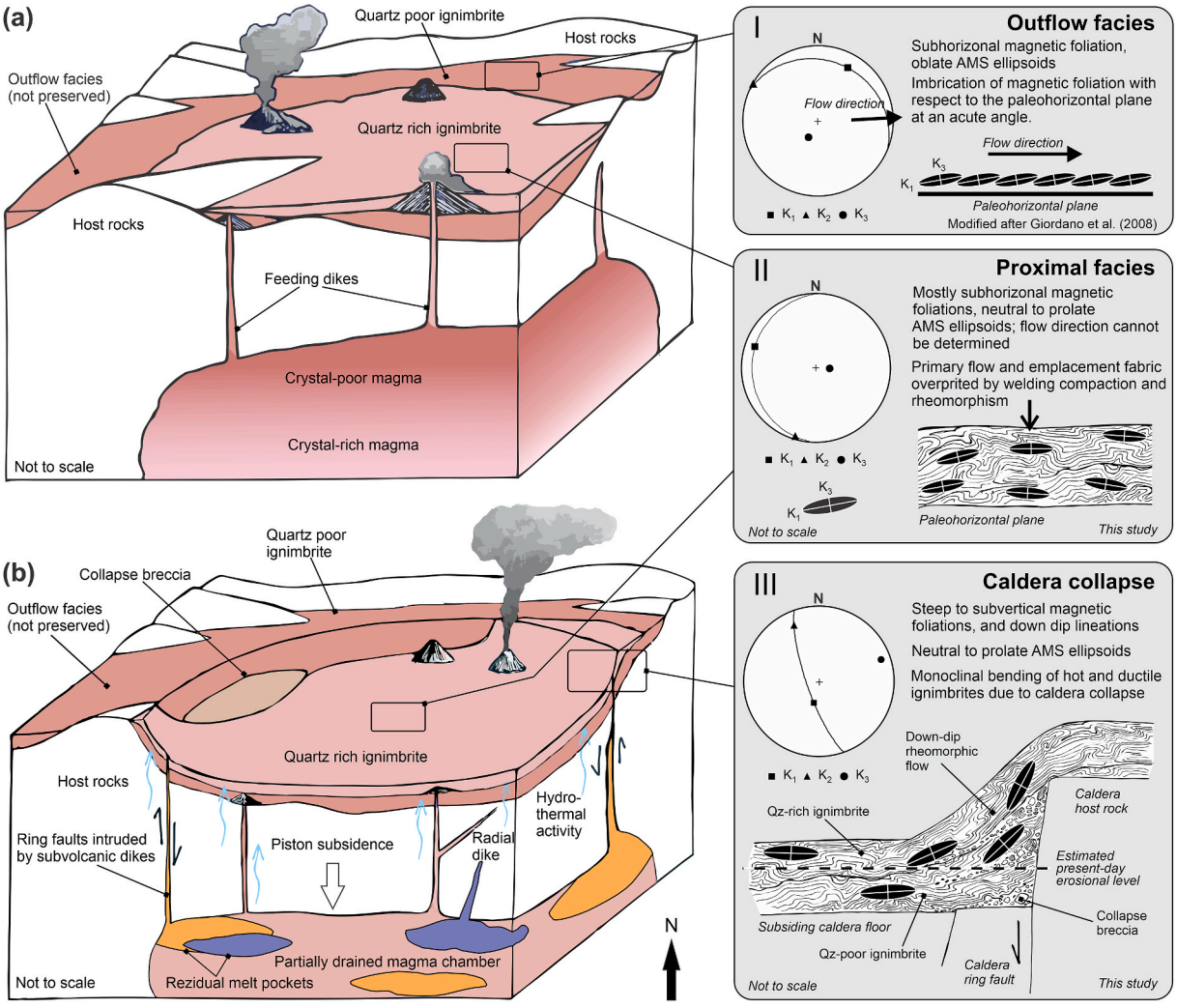

Fig. 12. Simplified model of the two-phase evolution of TWC based on fabric patterns of the ignimbrites. (a) Caldera-forming eruptions sourced the pyroclastic flows deposited on the pre-caldera topography. (b) Piston-style caldera collapse following the drainage of the underlying magma chamber. Note the expected fabric pattern for proximal and outflow facies in the right panels. The strike of magnetic foliations and plunge of lineations in the stereographic projections may vary across the caldera depending on the hypothetical sampling site.

syn-emplacement ductile rheomorphic deformation (Fig. 12b). Welding compaction and rheomorphism transposed the primary depositional and emplacement structures forming the subhorizontal to shallowly plunging fabrics with prolate ellipsoids and sheared eutaxitic microstructure (e.g., Seaman et al., 1991; Wang et al., 2001), although locally some sites preserved likely a primary emplacement-related oblate fabric.

Following the eruption, the caldera collapsed due to the drainage of the underlying magma chamber resulting in the partial collapse of caldera walls and emplacement of the collapse breccia (Breitkreuz et al., 2021). The caldera collapse occurred when the ignimbrite was still hot and ductile, allowing the reorientation of foliations and lineations in a hypersolidus state. The fabrics rotated down-dip towards the caldera center yielding a pattern of steep fabrics encircling the caldera rim (Fig. 12). Late-stage caldera activity was marked by the intrusion of subvolcanic ring dikes and other minor intrusions (Benek, 1980; Breitkreuz et al., 2021). The post-emplacement hydrothermal activity of the subvolcanic magmatic system likely caused the alteration of magnetic mineralogy (Fig. 12b).

7.3. Magnetic fabrics of ignimbrites: short methodological remarks

Perhaps the biggest methodological issue is that the recent papers showed that opAMS may be used instead of AARM in some cases or the opAMS results resemble those of AARM, and field- and frequency-dependent AMS in subvolcanic dikes (Hrouda et al., 2017, 2020). This ignimbrite study, however, reports several sites, where opAMS and AARM principal axes are non-coaxial, while the AARM foliations are parallel with flow foliation measured in the field. We speculate that such a disbalance is caused by the random orientation of minerals (subfabrics) that carry the opAMS and AARM signal. Only in cases, where the opAMS reflect the fabric of ultrafine magnetite grains that are parallel to larger magnetite grains (i.e., vortex state and/or multi-domain), the opAMS can be used instead of the AARM. Therefore, detailed magneto-mineralogical analyses are necessary to be conducted before analyzing the overall magnetic fabric pattern.

Our dataset corroborates that the ipAMS represent a stand-alone method for interpreting the magma flow and fabrics of ignimbrite deposit (Hrouda, 1982; Tarling and Hrouda, 1993; Borradaile and Henry, 1997; Borradaile and Jackson, 2004, 2010; Chadima et al., 2009; Agrò et al., 2015). Our cautionary note on magnetic fabrics methodology is only related to deeply eroded caldera ignimbrites that are in part altered by hydrothermal fluids due to the activity of the post-caldera magmatic system or some later events. Such processes may potentially lead to the evolution of inverse and/or composite (sub)fabric that potentially bias the fabric interpretation. The application of magnetic multi-fabrics as exemplified in this study may reveal composite fabrics that should be considered with caution in geodynamic interpretations of magnetic fabrics. Alternatively, the detection of composite fabrics offers other opportunities to investigate the alteration processes of magnetic mineralogy in greater detail (Just et al., 2004; Gee et al., 2010; Petronis et al., 2011; Kontny and Dietze, 2014).

8. Conclusions

The field mapping, petrography, flow foliation pattern, rock-magnetic analyses, and magnetic fabrics from various techniques of TWC rhyolitic ignimbrites indicate a two-stage caldera evolution. First, the PDC filled the erosional paleodepressions to form a thick ignimbrite sheet. The highly energetic and hot PDCs caused a high degree of welding and rheomorphism in the proximal part of the caldera. Simultaneously, the caldera-forming eruptions emptied the underlying source magma chamber and triggered a collapse. Second, the welded hot and ductile ignimbrite sheet commenced monoclinal bending downwards in response to piston subsidence causing the transposition of primary emplacement hypersolidus fabrics to steep inward dipping fabric encircling the caldera rim. The caldera collapse is postdated by the intrusion of microgranite ring and radial dikes associated with a high heat and hydrothermal fluid flow. The latter likely caused late-stage magmatic and/or secondary alteration of the magnetic mineralogy as revealed by multiple rock magnetic techniques. To avoid a possible ipAMS bias caused by composite (sub)fabrics and unorganized magnetic fabrics that transposed the primary emplacement record, a multi-fabric approach (ipAMS, opAMS, and AARM) was employed. Moreover, our results indicate that the opAMS may substitute the AARM only in the case when the shape-preferred orientation of ultrafine magnetite grains is parallel to single-domain, vortex state, and multi-domain grains. This can be only distinguished by the application of detailed magneto-mineralogical tests identifying the magnetic domain states. Therefore, we suggest that in contrast with young and well-exposed ignimbrites, the complex intra-caldera ignimbrite deposits, including welded to rheomorphic domains and those located in highly eroded or poorly exposed terrains, should be investigated via multiple magnetic methods.

Funding

This study was supported by the Grant Agency of Charles University project No. 124320 (Olšanská), Czech Science Foundation junior grant No.19-02177Y (Tomek), Charles University projects Cooperatio Programme (Research Area GEOL) and Centre for Geosphere Dynamics (UNCE/SCI/006), and Institute of Geology (Czech Academy of Sciences) institutional support RVO6798583. Hysteresis and FORC analyses were supported by National Science Foundation grants DMR-1523611 and DMR-2122108 (PREM) awarded to Drs. T. Timofeeva and G. Gallegos at New Mexico Highlands University. Petronis acknowledges the Fulbright program, which funded his visiting fellowship at Charles University in 2022.

Declaration of competing interest

The authors declare no competing interests.

Data availability

Data will be made available on request.

Acknowledgments

We gratefully acknowledge the constructive comments by Claudio Robustelli Test and an anonymous referee as well as the careful editorial handling by Ian Alsop. This study is a part of the Ph.D. project of Irena Olšanská. Christoph Breitkreuz is thanked for introducing us to the field area. Fritz Finger and Christoph von Hagke are thanked for the discussions. Petr Vitouš is thanked for help with fieldwork. We acknowledge Manuel Lapp and Saxony State Office for the Environment Agriculture and Geology for providing us with the forest entry permit. We are indebted to the following colleagues who provided technical support, namely Rudolf Trnka, Martin Racek, Jiří Petráček, Milena Vostrá, and Simona Horychová.

Appendix A. Supplementary data

Supplementary data to this article can be found online at https://doi.org/10.1016/j.jsg.2023.105012.

References

Ade-Hall, J.M., Palmer, H.C., Hubbard, T.P., 1971. The magnetic and opaque petrological response of basalts to regional hydrothermal alteration. Geophys. J. Int. 24, 137–174. https://doi.org/10.1111/j.1365-246X.1971.tb02171.x.

Agrò, A., Zanella, E., Le Pennec, J.L., Temel, A., 2015. Magnetic fabric of ignimbrites: a case study from the Central Anatolian Volcanic Province. In: Ort, M.H., Porreca, M., Geissman, J.W. (Eds.), The Use of Palaeomagnetism and Rock Magnetism to

Understand Volcanic Processes, 396. Geol. Soc. London Spec. Publ., pp. 159–175. https://doi.org/10.1144/SP396.9
Akkoyun, M., Majesté, J.-C., Bascou, J., 2013. Using the anisotropy of magnetic susceptibility to infer flow-induced orientation of anisotropic particles: feasibility and sensitivity. Rheol. Acta 52, 49–57. https://doi.org/10.1007/s00397-012-0670-6.
Aleksandrowski, P., 1997. Kinematic data on major Variscan strike-slip faults and shear zones in the Polish Sudetes, northeast Bohemian Massif. Geol. Mag. 134, 727–739. https://doi.org/10.1017/S0016756897007590.
Baer, E.M., Fisher, R.V., Fuller, M., Valentine, G., 1997. Turbulent transport and deposition of the Ito pyroclastic flow: determinations using anisotropy of magnetic susceptibility. J. Geophys. Res. Solid Earth 102, 22565–22586. https://doi.org/10.1029/96JB01277.
Benek, R., 1980. Geologisch-strukturelle Untersuchungen im Tharandter Vulkanitkomplex (Suedteil DDR). Z. Geol. Wiss. 8, 627–643.
Borradaile, G.J., 1987. Anisotropy of magnetic susceptibility: rock composition versus strain. Tectonophysics 138, 327–329. https://doi.org/10.1016/0040-1951(87)90051-5.
Borradaile, G.J., 1991. Correlation of strain with anisotropy of magnetic susceptibility (AMS). Pure Appl. Geophys. 135, 15–29. https://doi.org/10.1007/BF00877006.
Borradaile, G.J., 2001. Magnetic fabrics and petrofabrics: their orientation distributions and anisotropies. J. Struct. Geol. 23, 1581–1596. https://doi.org/10.1016/S0191-8141(01)00019-0.
Borradaile, G.J., Werner, T., 1994. Magnetic anisotropy of some phyllosilicates. Tectonophysics 235, 223–248. https://doi.org/10.1016/0040-1951(94)90196-1.
Borradaile, G.J., Henry, B., 1997. Tectonic applications of magnetic susceptibility and its anisotropy. Earth Sci. Rev. 42, 49–93. https://doi.org/10.1016/s0012-8252(96)00044-x.
Borradaile, G.J., Gauthier, D., 2003. Interpreting anomalous magnetic fabrics in ophiolite dikes. J. Struct. Geol. 25, 171–182. https://doi.org/10.1016/s0191-8141(02)00025-1.
Borradaile, G.J., Jackson, M., 2004. Anisotropy of magnetic susceptibility (AMS): Magnetic petrofabrics of deformed rocks. In: Martín-Hernández, F., Lüneberg, C.M., Aubourg, C., Jackson, M. (Eds.), Magnetic Fabric: Methods and Applications. Geol. Soc. London Spec. Publ, vol. 238, pp. 299–360. https://doi.org/10.1144/gsl.Sp.2004.238.01.18.
Borradaile, G.J., Jackson, M., 2010. Structural geology, petrofabrics and magnetic fabrics (AMS, AARM, AIRM). J. Struct. Geol. 32, 1519–1551. https://doi.org/10.1016/j.jsg.2009.09.006.
Branney, M.J., Kokelaar, P., 2007. Pyroclastic Density Currents and the Sedimentation of Ignimbrites. In: Geol. Soc. London Mem, vol. 27. https://doi.org/10.1144/GSL.MEM.2003.027.
Breitkreuz, C., Käßner, A., Tichomirowa, M., Lapp, M., Huang, S., Stanek, K., 2021. The Late Carboniferous deeply eroded Tharandt Forest caldera–Niederbobritzsch granite complex: a post-Variscan long-lived magmatic system in central Europe. Int. J. Earth Sci. 110, 1265–1292. https://doi.org/10.1007/s00531-021-02015-x.
Burchardt, S., Mattsson, T., Palma, J.O., Galland, O., Almqvist, B., Mair, K., Jerram, D.A., Hammer, Ø., Sun, Y., 2019. Progressive growth of the Cerro Bayo Cryptodome, Chachahuén volcano, Argentina—implications for viscous magma emplacement. J. Geophys. Res. Solid Earth 124, 7934–7961. https://doi.org/10.1029/2019JB017543.
Cagnoli, B., Tarling, D.H., 1997. The reliability of anisotropy of magnetic susceptibility (AMS) data as flow direction indicators in friable base surge and ignimbrite deposits: Italian examples. J. Volcanol. Geoth. Res. 75, 309–320. https://doi.org/10.1016/S0377-0273(96)00038-8.
Cañón-Tapia, E., 1996. Single-grain versus distribution anisotropy: a simple three-dimensional model. Phys. Earth Planet. In. 94, 149–158. https://doi.org/10.1016/0031-9201(95)03072-7.
Černý, J., Melichar, R., Všianský, D., Drahokoupil, J., 2020. Magnetic anisotropy of rocks: a new classification of inverse magnetic fabrics to help geological interpretations. J. Geophys. Res. Solid Earth 125, e2020JB020426. https://doi.org/10.1029/2020JB020426.
Chadima, M., Cajz, V., Týcová, P., 2009. On the interpretation of normal and inverse magnetic fabric in dikes: examples from the Eger Graben, NW Bohemian Massif. Tectonophysics 466, 47–63. https://doi.org/10.1016/j.tecto.2008.09.005.
Cruz, C., Sant'Ovaia, H., McCarthy, W., Noronha, F., 2022. Anisotropy of out-of-phase magnetic susceptibility: a non-standard approach for magnetic subfabrics determination in Variscan Granites of Iberian Massif. Minerals 12, 1376. https://doi.org/10.3390/MIN12111376.
Day, R., Fuller, M., Schmidt, V.A., 1977. Hysteresis properties of titanomagnetites: grain-size and compositional dependence. Phys. Earth Planet. In. 13, 260–267. https://doi.org/10.1016/0031-9201(77)90108-x.
Dearing, J.A., Dann, R.J.L., Hay, K., Lees, J.A., Loveland, P.J., Maher, B.A., O'Grady, K., 1996. Frequency-dependent susceptibility measurements of environmental materials. Geophys. J. Int. 124, 228–240. https://doi.org/10.1111/j.1365-246X.1996.tb06366.x.
Dörr, W., Zulauf, G., 2010. Elevator tectonics and orogenic collapse of a Tibetan-style plateau in the European Variscides: the role of the Bohemian shear zone. Int. J. Earth Sci. 99, 299–325. https://doi.org/10.1007/s00531-008-0389-x.
Druitt, T.H., 1998. Pyroclastic Density Currents. In: Gilbert, J.S., Sparks, R.S.J. (Eds.), The Physics of Explosive Volcanic Eruptions, vol. 145, pp. 145–182. https://doi.org/10.1144/GSL.SP.1996.145.01.08. Geol. Soc. London Spec. Publ.
Dufek, J., Esposti Ongaro, T., Roche, O., 2015. Pyroclastic density currents: processes and models. In: Sigurdsson, H. (Ed.), The Encyclopedia of Volcanoes. Academic Press, Elsevier, pp. 617–629. https://doi.org/10.1016/B978-0-12-385938-9.00035-3.
Dunlop, D.J., Özdemir, Ö., 1997. Rock Magnetism. Cambridge University Press. https://doi.org/10.1017/CBO9780511612794.
Edel, J.B., Schulmann, K., Skrzypek, E., Cocherie, A., 2013. Tectonic evolution of the European Variscan belt constrained by palaeomagnetic, structural and anisotropy of magnetic susceptibility data from the Northern Vosges magmatic arc (eastern France). J. Geol. Soc. 170, 785–804. https://doi.org/10.1144/jgs2011-138.
Edel, J.B., Schulmann, K., Lexa, O., Lardeaux, J.M., 2018. Late Palaeozoic palaeomagnetic and tectonic constraints for amalgamation of Pangea supercontinent in the European Variscan belt. Earth Sci. Rev. 177, 589–612. https://doi.org/10.1016/j.earscirev.2017.12.007.
Ellwood, B.B., 1982. Estimates of flow direction for calc-alkaline welded tuffs and paleomagnetic data reliability from anisotropy of magnetic susceptibility measurements: central San Juan Mountains, southwest Colorado. Earth Planet Sci. Lett. 59, 303–314. https://doi.org/10.1016/0012-821X(82)90133-9.
Eyre, J.K., 1997. Frequency dependence of magnetic susceptibility for populations of single-domain grains. Geophys. J. Int. 129, 209–211. https://doi.org/10.1111/j.1365-246X.1997.tb00951.x.
Ferré, E.C., 2002. Theoretical models of intermediate and inverse AMS fabrics. Geophys. Res. Lett. 29 https://doi.org/10.1029/2001GL014367, 31-1–31-4.
Finger, F., Gerdes, A., René, M., Riegler, G., 2009. The Saxo-Danubian Granite Belt: magmatic response to post-collisional delamination of mantle lithosphere below the southwestern sector of the Bohemian Massif (Variscan orogen). Geol. Carpathica 60, 205–212. https://doi.org/10.2478/v10096-009-0014-3.
Finger, F., Schiller, D., Lindner, M., Hauzenberger, C., Verner, K., Žák, J., 2022. Ultrahigh-temperature granites and a curious thermal eye in the post-collisional South Bohemian batholith of the Variscan orogenic belt (Europe). Geology 50, 542–546. https://doi.org/10.1130/g49645.1.
Fisher, R.V., Orsi, G., Ort, M., Heiken, G., 1993. Mobility of a large-volume pyroclastic flow - emplacement of the Campanian ignimbrite, Italy. J. Volcanol. Geoth. Res. 56, 205–220. https://doi.org/10.1016/0377-0273(93)90017-L.
Förster, H.J., Tischendorf, G., Trumbull, R.B., Gottesmann, B., 1999. Late-collisional granites in the Variscan Erzgebirge, Germany. J. Petrol. 40, 1613–1645. https://doi.org/10.1093/petroj/40.11.1613.
Franke, W., 1989. Variscan plate tectonics in Central Europe-current ideas and open questions. Tectonophysics 169, 221–228. https://doi.org/10.1016/0040-1951(89)90088-7.
Franke, W., 2006. The Variscan orogen in Central Europe: Construction and collapse. In: Gee, D.G., Stephenson, R.A. (Eds.), European Lithosphere Dynamics. Geol. Soc. London Mem, vol. 32, pp. 333–343. https://doi.org/10.1144/GSL.MEM.2006.032.01.20.
Gee, J.S., Yu, Y., Bowes, J., 2010. Paleointensity estimates from ignimbrites: an evaluation of the Bishop Tuff. Geochem., Geophys., Geosyst. 11, Q03010 https://doi.org/10.1029/2009GC002834.
Gehmlich, M., Linnemann, U., Tichomirowa, M., Todt, W., Bombach, K., 2000. U-Pb- and Pb-Pb-zircon dating on metaigneous rocks of the Elbe Zone: consequences for the Variscan nappe stacking in the Saxothuringian domain. Z. Dtsch. Geol. Ges. 151, 209–230. https://doi.org/10.1127/zdgg/151/2000/209.
Geissman, J.W., Holm, D., Harlan, S.S., Embree, G.F., 2010. Rapid, high-temperature formation of large-scale rheomorphic structures in the 2.06 Ma Huckleberry Ridge Tuff, Idaho, USA. Geology 38, 263–266. https://doi.org/10.1130/G30492.1.
Gerdes, A., Wörner, G., Henk, A., 2000. Post-collisional granite generation and HT-LP metamorphism by radiogenic heating: the Variscan South Bohemian Batholith. J. Geol. Soc. 157, 577–587. https://doi.org/10.1144/jgs.157.3.577.
Giordano, G., Cas, R.A.F., 2021. Classification of ignimbrites and their eruptions. Earth Sci. Rev. 220, 103697 https://doi.org/10.1016/j.earscirev.2021.103697.
Giordano, G., Porreca, M., Musacchio, P., Mattei, M., 2008. The Holocene Secche di Lazzaro phreatomagmatic succession (Stromboli, Italy): evidence of pyroclastic density current origin deduced by facies analysis and AMS flow directions. Bull. Volcanol. 70, 1221–1236. https://doi.org/10.1007/s00445-008-0198-x.
Gountié Dedzo, M., Nédélec, A., Nono, A., Njanko, T., Font, E., Kamgang, P., Njonfang, E., Launeau, P., 2011. Magnetic fabrics of the Miocene ignimbrites from West-Cameroon: implications for pyroclastic flow source and sedimentation. J. Volcanol. Geoth. Res. 203, 113–132. https://doi.org/10.1016/j.jvolgeores.2011.04.012.
Hargraves, R.B., Johnson, D., Chan, C.Y., 1991. Distribution anisotropy: the cause of AMS in igneous rocks? Geophys. Res. Lett. 18, 2193–2196. https://doi.org/10.1029/91GL01777.
Harrison, R.J., Feinberg, J.M., 2009. Mineral magnetism: providing new insights into geoscience processes. Elements 5, 209–215. https://doi.org/10.2113/gselements.5.4.209.
Hoffmann, U., Breitkreuz, C., Breiter, K., Sergeev, S., Stanek, K., Tichomirowa, M., 2013. Carboniferous-Permian volcanic evolution in Central Europe-U/Pb ages of volcanic rocks in Saxony (Germany) and northern Bohemia (Czech Republic). Int. J. Earth Sci. 102, 73–99. https://doi.org/10.1007/s00531-012-0791-2.
Housen, B.A., Richter, C., van der Pluijm, B.A., 1993. Composite magnetic anisotropy fabrics: experiments, numerical models and implications for the quantification of rock fabrics. Tectonophysics 220, 1–12. https://doi.org/10.1016/0040-1951(93)90219-A.
Hrouda, F., 1982. Magnetic anisotropy of rocks and its application in geology and geophysics. Geophys. Surv. 5, 37–82. https://doi.org/10.1007/BF01450244.
Hrouda, F., 1994. A technique for the measurement of thermal changes of magnetic susceptibility of weakly magnetic rocks by the CS-2 apparatus and KLY-2 Kappabridge. Geophys. J. Int. 118, 604–612. https://doi.org/10.1111/j.1365-246X.1994.tb03987.x.
Hrouda, F., 2002a. The use of the anisotropy of magnetic remanence in the resolution of the anisotropy of magnetic susceptibility into its ferromagnetic and paramagnetic

components. Tectonophysics 347, 269–281. https://doi.org/10.1016/S0040-1951(02)00075-6.
Hrouda, F., 2002b. Low-field variation of magnetic susceptibility and its effect on the anisotropy of magnetic susceptibility of rocks. Geophys. J. Int. 150, 715–723. https://doi.org/10.1046/j.1365-246X.2002.01731.x.
Hrouda, F., 2011. Models of frequency-dependent susceptibility of rocks and soils revisited and broadened. Geophys. J. Int. 187, 1259–1269. https://doi.org/10.1111/j.1365-246X.2011.05227.x.
Hrouda, F., Jelínek, V., 1990. Resolution of ferrimagnetic and paramagnetic anisotropies in rocks, using combined low-field and high-field measurements. Geophys. J. Int. 103, 75–84. https://doi.org/10.1111/j.1365-246X.1990.tb01753.x.
Hrouda, F., Ježek, J., 2014. Frequency-dependent AMS of rocks: a tool for the investigation of the fabric of ultrafine magnetic particles. Tectonophysics 629, 27–38. https://doi.org/10.1016/j.tecto.2014.01.040.
Hrouda, F., Jelínek, V., Zapletal, K., 1997. Refined technique for susceptibility resolution into ferromagnetic and paramagnetic components based on susceptibility temperature-variation measurement. Geophys. J. Int. 129, 715–719. https://doi.org/10.1111/j.1365-246X.1997.tb04506.x.
Hrouda, F., Chlupáčová, M., Mrázová, Š., 2006. Low-field variation of magnetic susceptibility as a tool for magnetic mineralogy of rocks. Phys. Earth Planet. In. 154, 323–336. https://doi.org/10.1016/j.pepi.2005.09.013.
Hrouda, F., Faryad, S.W., Chlupáčová, M., Jeřábek, P., Kratinová, Z., 2009. Determination of field-independent and field-dependent components of anisotropy of susceptibility through standard AMS measurement in variable low fields II: an example from the ultramafic body and host granulitic rocks at Bory in the Moldanubian Zone of Western Moravia, Czech Republic. Tectonophysics 466, 123–134. https://doi.org/10.1016/j.tecto.2008.10.014.
Hrouda, F., Pokorný, J., Ježek, J., Chadima, M., 2013. Out-of-phase magnetic susceptibility of rocks and soils: a rapid tool for magnetic granulometry. Geophys. J. Int. 194, 170–181. https://doi.org/10.1093/gji/ggt097.
Hrouda, F., Chadima, M., Ježek, J., Pokorný, J., 2017. Anisotropy of out-of-phase magnetic susceptibility of rocks as a tool for direct determination of magnetic subfabrics of some minerals: an introductory study. Geophys. J. Int. 208, 385–402. https://doi.org/10.1093/gji/ggw399.
Hrouda, F., Chadima, M., Ježek, J., Kadlec, J., 2018a. Anisotropies of in-phase, out-of-phase, and frequency-dependent susceptibilities in three loess/palaeosol profiles in the Czech Republic; methodological implications. Studia Geophys. Geod. 62, 272–290. https://doi.org/10.1007/s11200-017-0701-y.
Hrouda, F., Gilder, S., Wack, M., Ježek, J., 2018b. Diverse response of paramagnetic and ferromagnetic minerals to deformation from Intra-Carpathian Palaeogene sedimentary rocks: comparison of magnetic susceptibility and magnetic remanence anisotropies. J. Struct. Geol. 113, 217–224. https://doi.org/10.1016/j.jsg.2018.06.001.
Hrouda, F., Ježek, J., Chadima, M., 2020. Anisotropy of out-of-phase magnetic susceptibility as a potential tool for distinguishing geologically and physically controlled inverse magnetic fabrics in volcanic dykes. Phys. Earth Planet. In. 307, 106551 https://doi.org/10.1016/j.pepi.2020.106551.
Hrouda, F., Chadima, M., Ježek, J., 2022. Anisotropy of out-of-phase magnetic susceptibility and its potential for rock fabric studies: a review. Geosciences 12, 234. https://doi.org/10.3390/geosciences12060234.
Jackson, M., 1991. Anisotropy of magnetic remanence: a brief review of mineralogical sources, physical origins, and geological applications, and comparison with susceptibility anisotropy. Pure Appl. Geophys. 136, 1–28. https://doi.org/10.1007/BF00878885.
Jackson, M., Moskowitz, B., Rosenbaum, J., Kissel, C., 1998. Field-dependence of AC susceptibility in titanomagnetites. Earth Planet Sci. Lett. 157, 129–139. https://doi.org/10.1016/S0012-821X(98)00032-6.
Janoušek, V., Hanžl, P., Svojtka, M., Hora, J.M., Erban Kochergina, Y.V., Gadas, P., Holub, F.V., Gerdes, A., Verner, K., Hrdličková, K., Daly, J.S., Buriánek, D., 2020. Ultrapotassic magmatism in the heyday of the Variscan Orogeny – the story of the Třebíč Pluton, the largest durbachitic body in the Bohemian Massif. Int. J. Earth Sci. 109, 1767–1810. https://doi.org/10.1007/s00531-020-01872-2.
Jelínek, V., 1978. Statistical processing of anisotropy of magnetic susceptibility measured on groups of specimens. Studia Geophys. Geod. 22, 50–62. https://doi.org/10.1007/BF01613632.
Jelínek, V., 1981. Characterization of the magnetic fabric of rocks. Tectonophysics 79, T63–T67. https://doi.org/10.1016/0040-1951(81)90110-4.
Just, J., Kontny, A., De Wall, H., Hirt, A.M., Martín-Hernández, F., 2004. Development of magnetic fabrics during hydrothermal alteration in the Soultz-sous-Forêts granite from the EPS-1 borehole, Upper Rhine Graben. In: Martín-Hernández, F., Lüneberg, C.M., Aubourg, C., Jackson, M. (Eds.), Magnetic Fabric: Methods and Applications. Geol. Soc. London Spec. Publ, vol. 238, pp. 509–526. https://doi.org/10.1144/gsl.Sp.2004.238.01.26.
Käßner, A., Tichomirowa, M., Lapp, M., Leonhardt, D., Whitehouse, M., Gerdes, A., 2021. Two-phase late Paleozoic magmatism (~313–312 and ~299–298 Ma) in the Lusatian Block and its relation to large scale NW striking fault zones: evidence from zircon U–Pb CA–ID–TIMS geochronology, bulk rock- and zircon chemistry. Int. J. Earth Sci. 110, 2923–2953. https://doi.org/10.1007/s00531-021-02092-y.
Knight, M.D., Walker, G.P.L., 1988. Magma flow directions in dikes of the Koolau Complex, Oahu, determined from magnetic fabric studies. J. Geophys. Res. Solid Earth 93, 4301–4319. https://doi.org/10.1029/jb093ib05p04301.
Kolářová, K., Černý, J., Melichar, R., Schnabl, P., Gaidzik, K., 2022. Reconstruction of ancient volcanic complexes using magnetic signature: a case study from Cambrian andesite lava flow, Bohemian Massif. J. Volcanol. Geoth. Res. 428, 107591 https://doi.org/10.1016/j.jvolgeores.2022.107591.
Kontny, A., Dietze, F., 2014. Magnetic fabrics in deformed metaperidotites of the Outokumpu Deep Drill Core, Finland: implications for a major crustal shear zone. Tectonophysics 629, 224–237. https://doi.org/10.1016/j.tecto.2014.04.011.
LaBerge, R.D., Porreca, M., Mattei, M., Giordano, G., Cas, R.A.F., 2009. Meandering flow of a pyroclastic density current documented by the anisotropy of magnetic susceptibility (AMS) in the quartz latite ignimbrite of the Pleistocene Monte Cimino volcanic centre (central Italy). Tectonophysics 466, 64–78. https://doi.org/10.1016/j.tecto.2008.09.009.
Lamarche, G., Froggatt, P.C., 1993. New eruptive vents for the Whakamaru ignimbrite (Taupo volcanic zone) identified from magnetic fabric study. N. Z. J. Geol. Geophys. 36, 213–222. https://doi.org/10.1080/00288306.1993.9514569.
Le Pennec, J.L., Chen, Y., Diot, H., Froger, J.L., Gourgaud, A., 1998. Interpretation of anistropy of magnetic susceptibility fabric of ignimbrites in terms of kinematic and sedimentological mechanisms: an Anatolian case-study. Earth Planet Sci. Lett. 157, 105–127. https://doi.org/10.1016/S0012-821X(97)00215-X.
Lindsay, J.M., De Silva, S., Trumbull, R., Emmermann, R., Wemmer, K., 2001. La Pacana caldera, N. Chile: a re-evaluation of the stratigraphy and volcanology of one of the world's largest resurgent calderas. J. Volcanol. Geoth. Res. 106, 145–173. https://doi.org/10.1016/S0377-0273(00)00270-5.
Lipman, P.W., 2007. Incremental assembly and prolonged consolidation of Cordilleran magma chambers: evidence from the Southern Rocky Mountain volcanic field. Geosphere 3, 42–70. https://doi.org/10.1130/GES00061.1.
Loock, S., Diot, H., Van Wyk de Vries, B., Launeau, P., Merle, O., Vadeboin, F., Petronis, M.S., 2008. Lava flow internal structure found from AMS and textural data: an example in methodology from the Chaîne des Puys, France. J. Volcanol. Geoth. Res. 177, 1092–1104. https://doi.org/10.1016/j.jvolgeores.2008.08.
MacDonald, W.D., Palmer, H.C., Deino, A.L., Shen, P.Y., 2012. Insights into deposition and deformation of intra-caldera ignimbrites, central Nevada. J. Volcanol. Geoth. Res. 245–246, 40–54. https://doi.org/10.1016/J.JVOLGEORES.2012.07.002.
Machac, T.A., Zanner, C.W., Geiss, C.E., 2007. Time dependent IRM acquisition as a tool to quantify the abundance of ultrafine superparamagnetic magnetite in loessic soils. Geophys. J. Int. 169, 483–489. https://doi.org/10.1111/j.1365-246X.2007.03355.x.
Martín-Hernández, F., Hirt, A.M., 2003. The anisotropy of magnetic susceptibility in biotite, muscovite and chlorite single crystals. Tectonophysics 367, 13–28. https://doi.org/10.1016/S0040-1951(03)00127-6.
Martínek, K., Pešek, J., Opluštil, S., 2017. Significant hiatuses in the terrestrial late Variscan central and western Bohemian basins (late Pennsylvanian-early Cisuralian) and their possible tectonic and climatic links. Geol. Carpathica 68, 269–281. https://doi.org/10.1515/geoca-2017-0019.
Matte, P., 1991. Accretionary history and crustal evolution of the Variscan belt in Western Europe. Tectonophysics 196, 309–337. https://doi.org/10.1016/0040-1951(91)90328-P.
Matte, P., Maluski, H., Rajlich, P., Franke, W., 1990. Terrane boundaries in the Bohemian Massif: result of large-scale Variscan shearing. Tectonophysics 177, 151–170. https://doi.org/10.1016/0040-1951(90)90279-H.
McCabe, 1985. Magnetic anisotropy in the Trenton Limestone: results of a new technique, anisotropy of anhysteretic susceptibility. Geophys. Res. Lett. 12, 333–336. https://doi.org/10.1029/GL012i006p00333.
Megerssa, L., Verner, K., Buriánek, D., Pour, O., Tomek, F., Schiller, D., Martínek, K., 2023. The late-Variscan high-temperature collisional episode in the southwestern Moldanubian Zone (Bohemian Massif). Int. J. Earth Sci. 112, 631–658. https://doi.org/10.1007/s00531-022-02258-2.
Moncinhatto, T.R., Haag, M.B., Hartmann, G.A., Savian, J.F., Poletti, W., Sommer, C.A., Caselli, A.T., Trindade, R.I.F., 2020. Mineralogical control on the magnetic anisotropy of lavas and ignimbrites: a case study in the Caviahue-Copahue field (Argentina). Geophys. J. Int. 220, 821–838. https://doi.org/10.1093/GJI/GGZ483.
Muxworthy, A.R., Mcclelland, E., 2000. Review of the low-temperature magnetic properties of magnetite from a rock magnetic perspective. Geophys. J. Int. 140, 101–114. https://doi.org/10.1046/j.1365-246x.2000.00999.x.
Nagata, T., 1961. Rock Magnetism. Tokyo, Maruzen.
Nédélec, A., Trindade, R., Peschler, A., Archanjo, C., Macouin, M., Poitrasson, F., Bouchez, J.L., 2015. Hydrothermally-induced changes in mineralogy and magnetic properties of oxidized A-type granites. Lithos 212 (215), 145–157. https://doi.org/10.1016/j.lithos.2014.11.007.
Nye, J.F., 1957. Physical properties of crystals: their representation by tensors and matrices. Clarendon Press, Oxford (Reprinted in 1985).
Opluštil, S., Cleal, C.J., 2007. A comparative analysis of some late carboniferous basins of Variscan Europe. Geol. Mag. 144, 417–448. https://doi.org/10.1017/S0016756807003330.
Opluštil, Stanislav, Schmitz, M., Cleal, C.J., Martínek, K., 2016a. A review of the Middle-Late Pennsylvanian west European regional substages and floral biozones, and their correlation to the Geological Time Scale based on new U-Pb ages. Earth Sci. Rev. 154, 301–335. https://doi.org/10.1016/j.earscirev.2016.01.004.
Opluštil, S., Schmitz, M., Kachlík, V., Štamberg, S., 2016b. Re-assessment of lithostratigraphy, biostratigraphy, and volcanic activity of the Late Paleozoic Intra-Sudetic, Krkonoše-Piedmont and Mnichovo Hradiště basins (Czech Republic) based on new U-Pb CA-ID-TIMS ages. Bull. Geosci. 91, 399–432. https://doi.org/10.3140/bull.geosci.1603.
Orlický, O., 1990. Detection of magnetic carriers in rocks: results of susceptibility changes in powdered rock samples induced by temperature. Phys. Earth Planet. In. 63, 66–70. https://doi.org/10.1016/0031-9201(90)90060-B.
Ort, M.H., Orsi, G., Pappalardo, L., Fisher, R.V., 2003. Anisotropy of magnetic susceptibility studies of depositional processes in the Campanian Ignimbrite, Italy. Bull. Volcanol. 65, 55–72. https://doi.org/10.1007/s00445-002-0241-2.
Ort, M.H., Newkirk, T.T., Vilas, J.F., Vazquez, J.A., 2015. Towards the definition of AMS facies in the deposits of pyroclastic density currents. In: Ort, M.H., Porreca, M.,

Geissman, J.W. (Eds.), The Use of Palaeomagnetism and Rock Magnetism to Understand Volcanic Processes. Geol. Soc. London Spec. Publ, vol. 396, pp. 205–226. https://doi.org/10.1144/SP396.8.

Paquereau-Lebti, P., Fornari, M., Roperch, P., Thouret, J.C., Macedo, O., 2008. Paleomagnetism, magnetic fabric, and 40Ar/39Ar dating of Pliocene and Quaternary ignimbrites in the Arequipa area, southern Peru. Bull. Volcanol. 70, 977–997. https://doi.org/10.1007/s00445-007-0181-y.

Petronis, M.S., Hacker, D.B., Holm, D.K., Geissmans, J.W., Harlan, S., 2004. Magmatic flow paths and palaeomagnetism of the Miocene Stoddard Mountain laccolith, Iron Axis Region. In: Martín-Hernández, F., Lüneberg, C.M., Aubourg, C., Jackson, M. (Eds.), Magnetic Fabric: Methods and Applications. Geol. Soc. London Spec. Publ, vol. 238, pp. 251–283. https://doi.org/10.1144/GSL.SP.2004.238.01.16.

Petronis, M.S., O'Driscoll, B., Lindline, J., 2011. Late stage oxide growth associated with hydrothermal alteration of the Western Granite, Isle of Rum, NW Scotland. Geochem., Geophys., Geosyst. 12, Q01001 https://doi.org/10.1029/2010GC003246.

Petrovský, E., Kapička, A., 2006. On determination of the Curie point from thermomagnetic curves. J. Geophys. Res. Solid Earth 111, B12S27. https://doi.org/10.1029/2006JB004507.

Pharaoh, T.C., 1999. Palaeozoic terranes and their lithospheric boundaries within the Trans-European Suture Zone (TESZ): a review. Tectonophysics 314, 17–41. https://doi.org/10.1016/S0040-1951(99)00235-8.

Pin, C., 1990. Variscan oceans: ages, origins and geodynamic implications inferred from geochemical and radiometric data. Tectonophysics 177, 215–227. https://doi.org/10.1016/0040-1951(90)90282-D.

Pioli, L., Lanza, R., Ort, M., Rosi, M., 2008. Magnetic fabric, welding texture and strain fabric in the Nuraxi Tuff, Sardinia, Italy. Bull. Volcanol. 70, 1123–1137. https://doi.org/10.1007/s00445-008-0194-1.

Platzman, E.S., Sparks, R.S.J., Cooper, F.J., 2020. Fabrics, facies, and flow through a large-volume ignimbrite: Pampa De Oxaya, Chile. Bull. Volcanol. 82, 1–19. https://doi.org/10.1007/s00445-019-1345-2.

Porreca, M., Mattei, M., Giordano, G., De Rita, D., Funiciello, R., 2003. Magnetic fabric and implications for pyroclastic flow and lahar emplacement, Albano maar, Italy. J. Geophys. Res. Solid Earth 108, 2264. https://doi.org/10.1029/2002jb002102.

Prival, J.-M., Harris, A.J.L., Zanella, E., Robustelli Test, C., Gurioli, L., Chevrel, O., Biren, J., 2022. Emplacement dynamics of a crystal-rich, highly viscous trachytic flow of the Sancy stratovolcano, France. GSA Bull. 135, 2057–2074. https://doi.org/10.1130/B36415.1.

Racek, M., Lexa, O., Schulmann, K., Corsini, M., Štípská, P., Maierová, P., 2017. Re-evaluation of polyphase kinematic and 40Ar/39Ar cooling history of Moldanubian hot nappe at the eastern margin of the Bohemian Massif. Int. J. Earth Sci. 106, 397–420. https://doi.org/10.1007/s00531-016-1410-4.

Richter, C., van Der Pluijm, B.A., Housen, B.A., 1993. The quantification of crystallographic preferred orientation using magnetic anisotropy. J. Struct. Geol. 15, 113–116. https://doi.org/10.1016/0191-8141(93)90082-L.

Roberts, A.P., Cui, Y., Verosub, K.L., 1995. Wasp-waisted hysteresis loops: mineral magnetic characteristics and discrimination of components in mixed magnetic systems. J. Geophys. Res. 100, 17909–17924. https://doi.org/10.1029/95JB00672.

Roberts, A.P., Pike, C.R., Verosub, K.L., 2000. First-order reversal curve diagrams: a new tool for characterizing the magnetic properties of natural samples. J. Geophys. Res. Solid Earth 105, 28461–28475. https://doi.org/10.1029/2000jb900326.

Roberts, A.P., Heslop, D., Zhao, X., Oda, H., Egli, R., Harrison, R.J., Hu, P., Muxworthy, A.R., Sato, T., 2022. Unlocking information about fine magnetic particle assemblages from first-order reversal curve diagrams: recent advances. Earth Sci. Rev. 227, 103950 https://doi.org/10.1016/j.earscirev.2022.103950.

Rochette, P., 1987. Magnetic susceptibility of the rock matrix related to magnetic fabric studies. J. Struct. Geol. 9, 1015–1020. https://doi.org/10.1016/0191-8141(87)90009-5.

Rochette, P., 1988. Inverse magnetic fabric in carbonate-bearing rocks. Earth Planet Sci. Lett. 90, 229–237. https://doi.org/10.1016/0012-821X(88)90103-3.

Rochette, P., Aubourg, C., Perrin, M., 1999. Is this magnetic fabric normal? A review and case studies in volcanic formations. Tectonophysics 307, 219–234. https://doi.org/10.1016/S0040-1951(99)00127-4.

Schäfer, J., Neuroth, H., Ahrendt, H., Dörr, W., Franke, W., 1997. Accretion and exhumation at a Variscan active margin, recorded in the Saxothuringian flysch. Geol. Rundsch. 86, 599–611. https://doi.org/10.1007/s005310050166.

Scheck, M., Bayer, U., Otto, V., Lamarche, J., Banka, D., Pharaoh, T.T., 2002. The Elbe fault system in North Central Europe - a basement controlled zone of crustal weakness. Tectonophysics 360, 281–299. https://doi.org/10.1016/S0040-1951(02)00357-8.

Schirnick, C., Van Den Bogaard, P., Schmincke, H.U., 1999. Cone sheet formation and intrusive growth of an oceanic island-the Miocene Tejeda complex on Gran Canaria (Canary Islands). Geology 27, 207–210. https://doi.org/10.1130/0091-7613(1999)027<0207:CSFAIG>2.3.CO;2.

Schlinger, C.M., Rosenbaum, J.G., Veblen, D.R., 1988. Fe-oxide microcrystals in welded tuff from southern Nevada: origin of remanence carriers by precipitation in volcanic glass. Geology 16, 556–559. https://doi.org/10.1130/0091-7613(1988)016<0556:Fomiwt>2.3.Co;2.

Schulmann, K., Gayer, R., 2000. A model for a continental accretionary wedge developed by oblique collision: the NE Bohemian Massif. J. Geol. Soc. 157, 401–416. https://doi.org/10.1144/jgs.157.2.401.

Schulmann, K., Konopásek, J., Janoušek, V., Lexa, O., Lardeaux, J.M., Edel, J.B., Štípská, P., Ulrich, S., 2009. An Andean type Palaeozoic convergence in the Bohemian Massif. Compt. Rendus Geosci. 341, 266–286. https://doi.org/10.1016/j.crte.2008.12.006.

Schulmann, K., Lexa, O., Janoušek, V., Lardeaux, J.M., Edel, J.B., 2014. Anatomy of a diffuse cryptic suture zone: an example from the Bohemian Massif, European Variscides. Geology 42, 275–278. https://doi.org/10.1130/G35290.1.

Seaman, S.J., McIntosh, W.C., Geissman, J.W., Williams, M.L., Elston, W.E., 1991. Magnetic fabrics of the Bloodgood canyon and Shelley peak tuffs, southwestern New Mexico: implications for emplacement and alteration processes. Bull. Volcanol. 53, 460–476. https://doi.org/10.1007/BF00258185.

Shcherbakov, V.P., Fabian, K., 2005. On the determination of magnetic grain-size distributions of superparamagnetic particle ensembles using the frequency dependence of susceptibility at different temperatures. Geophys. J. Int. 162, 736–746. https://doi.org/10.1111/j.1365-246X.2005.02603.x.

Simón-Muzás, A., Casas-Sainz, A.M., Soto, R., Gisbert, J., Román-Berdiel, T., Oliva-Urcia, B., Pueyo, E.L., Beamud, E., 2022. Axial longitudinal flow in volcanic materials of the Late Carboniferous-Permian Cadí basin (Southern Pyrenees) determined from anisotropy of magnetic susceptibility. J. Volcanol. Geoth. Res. 421, 107443 https://doi.org/10.1016/j.jvolgeores.2021.107443.

Soler, M.M., Caffe, P.J., Coira, B.L., Onoe, A.T., Kay, S.M., 2007. Geology of the Vilama caldera: a new interpretation of a large-scale explosive event in the Central Andean plateau during the Upper Miocene. J. Volcanol. Geoth. Res. 164, 27–53. https://doi.org/10.1016/j.jvolgeores.2007.04.002.

Sparks, R.S.J., Self, S., Walker, G.P.L., 1973. Products of ignimbrite eruptions. Geology 1, 115–118. https://doi.org/10.1130/0091-7613(1973)1<115:POIE>2.0.CO;2.

Stephenson, A., 1994. Distribution anisotropy: two simple models for magnetic lineation and foliation. Phys. Earth Planet. In. 82, 49–53. https://doi.org/10.1016/0031-9201(94)90101-5.

Tarling, D., Hrouda, F., 1993. The Magnetic Anisotropy of Rocks. Chapman & Hall, London.

Tichomirowa, M., Berger, H.J., Koch, E.A., Belyatski, B.V., Götze, J., Kempe, U., Nasdala, L., Schaltegger, U., 2001. Zircon ages of high-grade gneisses in the eastern Erzgebirge (central European Variscides)—constraints on origin of the rocks and Precambrian to Ordovician magmatic events in the Variscan foldbelt. Lithos 56, 303–332. https://doi.org/10.1016/S0024-4937(00)00066-9.

Tichomirowa, M., Sergeev, S., Berger, H.J., Leonhardt, D., 2012. Inferring protoliths of high-grade metamorphic gneisses of the Erzgebirge using zirconology, geochemistry and comparison with lower-grade rocks from Lusatia (Saxothuringia, Germany). Contrib. Mineral. Petrol. 164, 375–396. https://doi.org/10.1007/S00410-012-0742-8.

Tichomirowa, M., Käßner, A., Sperner, B., Lapp, M., Leonhardt, D., Linnemann, U., Münker, C., Ovtcharova, M., Pfänder, J.A., Schaltegger, U., Sergeev, S., von Quadt, A., Whitehouse, M., 2019. Dating multiply overprinted granites: the effect of protracted magmatism and fluid flow on dating systems (zircon U-Pb: SHRIMP/SIMS, LA-ICP-MS, CA-ID-TIMS; and Rb–Sr, Ar–Ar) – granites from the Western Erzgebirge (Bohemian Massif, Germany). Chem. Geol. 519, 11–38. https://doi.org/10.1016/j.chemgeo.2019.04.024.

Tichomirowa, M., Käßner, A., Repstock, A., Weber, S., Gerdes, A., Whitehouse, M., 2022. New CA-ID-TIMS U–Pb zircon ages for the Altenberg–Teplice volcanic complex (ATVC) document discrete and coeval pulses of Variscan magmatic activity in the eastern Erzgebirge (eastern Variscan belt). Int. J. Earth Sci. 111, 1885–1908. https://doi.org/10.1007/S00531-022-02204-2.

Tomek, F., Žák, J., Holub, F.V., Chlupáčová, M., Verner, K., 2016. Growth of intra-caldera lava domes controlled by various modes of caldera collapse, the Štiavnica volcano-plutonic complex, Western Carpathians. J. Volcanol. Geoth. Res. 311, 183–197. https://doi.org/10.1016/j.jvolgeores.2016.01.006.

Tomek, F., Žák, J., Svojtka, M., Finger, F., Waitzinger, M., 2019. Emplacement dynamics of syn-collapse ring dikes: an example from the Altenberg–Teplice caldera, Bohemian Massif. GSA Bull. 131, 997–1016. https://doi.org/10.1130/B35019.1.

Tomek, F., Opluštil, S., Svojtka, M., Špillar, V., Rapprich, V., Míková, J., 2022. Altenberg–Teplice Caldera sourced Westphalian fall tuffs in the central and western Bohemian Carboniferous basins (eastern Variscan belt). Int. Geol. Rev. 64, 441–468. https://doi.org/10.1080/00206814.2020.1858357.

Tomek, F., Olšanská, I., Trubač, J., Černý, J., Rejšek, J., Ackerman, L., 2023. On the anatomy and structural control of a dyke swarm that fed caldera-forming ignimbrite eruptions. J. Geol. Soc. 180, jgs2022–j2119. https://doi.org/10.1144/jgs2022-119.

Tröger, K.A., Behr, H.J., Reichel, W., 1968. Die tektonische Entwicklung des Elbe-Lineaments im Bereich der Elbtalzone. Freiberger Forschungshefte Reihe C 241, 71–85 [in German].

Ulrych, J., Pešek, J., Štepánková-Svobodova, J., Bosák, P., Lloyd, F.E., von Seckendorff, V., Lang, M., Novák, J.K., 2006. Permo-Carboniferous volcanism in late Variscan continental basins of the Bohemian Massif (Czech Republic): geochemical characteristic. Chem. Erde 66, 37–56. https://doi.org/10.1016/j.chemer.2004.02.001.

Verner, K., Žák, J., Šrámek, J., Paclíková, J., Zavřelová, A., Machek, M., Finger, F., Johnson, K., 2014. Formation of elongated granite–migmatite domes as isostatic accommodation structures in collisional orogens. J. Geodyn. 73, 100–117. https://doi.org/10.1016/j.jog.2013.10.002.

Vitouš, P., Tomek, F., Petronis, M.S., 2022. Magnetic fabrics of rhyolite ignimbrites reveal complex emplacement dynamics of pyroclastic density currents, an example from the Altenberg–Teplice Caldera, Bohemian Massif. Bull. Volcanol. 84, 75. https://doi.org/10.1007/S00445-022-01577-1.

Walker, G.P.L., 1983. Ignimbrite types and ignimbrite problems. J. Volcanol. Geoth. Res. 17, 65–88. https://doi.org/10.1016/0377-0273(83)90062-8.

Wang, X., Roberts, J., Schmidt, P., 2001. Flow directions of carboniferous ignimbrites, Southern New England Orogen, Australia, using anisotropy of magnetic susceptibility. J. Volcanol. Geoth. Res. 110, 1–25. https://doi.org/10.1016/S0377-0273(01)00218-9.

Willcock, M.A.W., Mattei, M., Hasalová, P., Giordano, G., Cas, R.A.F., Morelli, C., 2015. Flow behaviour in the intra-caldera setting: An AMS study of the large (>1290 km3) Permian Ora ignimbrite. In: Ort, M.H., Porreca, M., Geissman, J.W. (Eds.), The Use of Palaeomagnetism and Rock Magnetism to Understand Volcanic Processes. Geol. Soc. London Spec. Publ, vol. 396, pp. 177–204. https://doi.org/10.1144/SP396.3.

Wilson, C.J.N., Walker, G.P.L., 1982. Ignimbrite depositional facies: the anatomy of a pyroclastic flow. J. Geol. Soc. 139, 581–592. https://doi.org/10.1144/GSJGS.139.5.0581.

Winchester, J.A., 2002. Palaeozoic amalgamation of Central Europe: new results from recent geological and geophysical investigations. Tectonophysics 360, 5–21. https://doi.org/10.1016/S0040-1951(02)00344-X.

Winchester, J.A., Pharaoh, T.C., Verniers, J., Ioane, D., Seghedi, A., 2006. Palaeozoic accretion of Gondwana-derived terranes to the East European craton: Recognition of detached terrane fragments dispersed after collision with promontories. In: Gee, D. G., Stephenson, R.A. (Eds.), European Lithosphere Dynamics. Geol. Soc. London Mem, vol. 32, pp. 323–332. https://doi.org/10.1144/GSL.MEM.2006.032.01.19.

Worm, H.U., 1998. On the superparamagnetic - stable single domain transition for magnetite, and frequency dependence of susceptibility. Geophys. J. Int. 133, 201–206. https://doi.org/10.1046/j.1365-246X.1998.1331468.x.

Žák, J., Holub, F.V., Verner, K., 2005. Tectonic evolution of a continental magmatic arc from transpression in the upper crust to exhumation of mid-crustal orogenic root recorded by episodically emplaced plutons: the Central Bohemian Plutonic Complex (Bohemian Massif). Int. J. Earth Sci. 94, 385–400. https://doi.org/10.1007/s00531-005-0482-3.

Žák, J., Verner, K., Finger, F., Faryad, S.W., Chlupáčová, M., Veselovský, F., 2011. The generation of voluminous S-type granites in the Moldanubian unit, Bohemian Massif, by rapid isothermal exhumation of the metapelitic middle crust. Lithos 121, 25–40. https://doi.org/10.1016/j.lithos.2010.10.002.

Žák, J., Verner, K., Holub, F.V., Kabele, P., Chlupáčová, M., Halodová, P., 2012. Magmatic to solid state fabrics in syntectonic granitoids recording early Carboniferous orogenic collapse in the Bohemian Massif. J. Struct. Geol. 36, 27–42. https://doi.org/10.1016/j.jsg.2011.12.011.

Žák, J., Verner, K., Sláma, J., Kachlík, V., Chlupáčová, M., 2013. Multistage magma emplacement and progressive strain accumulation in the shallow-level Krkonoše-Jizera plutonic complex, Bohemian Massif. Tectonics 32, 1493–1512. https://doi.org/10.1002/tect.20088.

Žák, J., Verner, K., Holub, F.V., Kachlík, V., Finger, F., Hajná, J., Tomek, F., Vondrovic, L., Trubač, J., 2014. A plate-kinematic model for the assembly of the Bohemian Massif constrained by structural relationships around granitoid plutons. In: Schulmann, K., Martínez Catalán, J.R., Lardeaux, J.M., Janoušek, V., Oggiano, G. (Eds.), The Variscan Orogeny: Extent, Timescale and the Formation of the European Crust. Geol. Soc. London Spec. Publ, vol. 405, pp. 169–196. https://doi.org/10.1144/SP405.

Závada, P., Schulmann, K., Lexa, O., Hrouda, F., Haloda, J., Týcová, P., 2009. The mechanism of flow and fabric development in mechanically anisotropic trachyte lava. J. Struct. Geol. 31, 1295–1307. https://doi.org/10.1016/J.JSG.2009.04.002.